Electrostatic flocking of salt-treated microfibers and nanofiber yarns for regenerative engineering

Alec McCarthy [a], Kossi Loic M. Avegnon [b], Phil A. Holubeck [a], Demi Brown [a], Anik Karan [a], Navatha Shree Sharma [a], Johnson V. John [a], Shelbie Weihs [a], Jazmin Ley [b], Jingwei Xie [a,b,*]

[a] Department of Surgery-Transplant and Mary & Dick Holland Regenerative Medicine Program, College of Medicine, University of Nebraska Medical Center, Omaha, NE, 668198, USA
[b] Department of Mechanical and Materials Engineering, College of Engineering, University of Nebraska-Lincoln, Lincoln, NE, 68588, USA

ARTICLE INFO

ABSTRACT

Electrostatic flocking is a textile technology that employs a Coulombic driving force to launch short fibers from a charging source towards an adhesive-covered substrate, resulting in a dense array of aligned fibers perpendicular to the substrate. However, electrostatic flocking of insulative polymeric fibers remains a challenge due to their insufficient charge accumulation. We report a facile method to flock electrostatically insulative poly(ε-caprolactone) (PCL) microfibers (MFs) and electrospun PCL nanofiber yarns (NFYs) by incorporating NaCl during pre-flock processing. Both MF and NFY were evaluated for flock functionality, mechanical properties, and biological responses. To demonstrate this platform's diverse applications, standalone flocked NFY and MF scaffolds were synthesized and evaluated as scaffold for cell growth. Employing the same methodology, scaffolds made from poly(glycolide-co-L-lactide) (PGLA) (90:10) MFs were evaluated for their wound healing capacity in a diabetic mouse model. Further, a flock-reinforced polydimethylsiloxane (PDMS) disc was fabricated to create an anisotropic artificial vertebral disc (AVD) replacement potentially used as a treatment for lumbar degenerative disc disease. Overall, a salt-based flocking method is described with MFs and NFYs, with wound healing and AVD repair applications presented.

1. Introduction

Creating highly porous and anisotropic objects for regenerative medicine and tissue engineering has remained a hallmark goal for several decades. Ideally, objects would retain high porosity and exhibit superb mechanical strength; however, this is rarely the case as highly porous materials (i.e., sponges or foams) have poor mechanical strengths and may be ill-suited in load bearing applications [1]. Increased efforts to generate anisotropic and highly porous biomaterials have resulted in new materials and techniques. For example, aligned 3D nanofiber objects, anisotropic aerogels, anisotropic and freeze-cast sponges, and electrostatically flocked objects have all demonstrated high porosities and salutary mechanical properties [2–7]. Notably, electrostatic flocking is a textile technology that uses an electrical field and Coulombic driving force to charge and launch fibers towards a substrate covered with an adhesive [8]. Electrostatic flocking typically consists of three components: short (micrometers to millimeters in length) fibers (flock fibers),

adhesives, and substrates [6]. Prior to flocking, fibers are sieved onto a charging electrode, where voltage is gradually applied until a sufficient charge is accumulated on the fiber surfaces. Once sufficient charging is achieved, the fibers are launched towards the ground electrode and embedded into an adhesive-covered substrate, leaving a forest of aligned fibers (Fig. S1) [9]. Fibers can be directly embedded into adhesives or cover the surface of an adhesive-covered substrate. Parameters such as flocking time, fibers sieved, fiber morphology, and applied voltage can be used to control fiber densities [6]. After fibers are sufficiently embedded, the adhesive/substrate can be easily removed from the ground electrode. Previous studies have optimized electrostatic flocking parameters including flock time, fiber length, and applied voltage and have demonstrated that fiber density and porosity can be easily controlled by flock time (the time a voltage is applied to the charging electrode) and fiber length [10,11]. These studies found that fiber density increased with flocking time and decreased with fiber length. Walther et al. found that 1 mm long fibers flocked for 5 and 15 s achieved fiber densities of 72

$\pm$ 11.2 and 104.5 $\pm$ 10.7 fibers/mm^2, respectively, while 3 mm fibers flocked for 5 and 15 s achieved only 11.4 $\pm$ 1.8 and 21.33 $\pm$ 3.3 fibers/mm^2, respectively [11].

Previously, electrostatic flocking has been used in tissue engineering as a fabrication technique to create porous and anisotropic structures for osteochondral engineering [6,10,11]. Noting the favorable in vitro and in vivo responses and tunable porosity and fiber density, flocked materials may offer an advantage over other tissue engineering and regenerative medicine approaches in some applications. The establishment of fully degradable flocked scaffolds using both chitosan and poly(-ε-caprolactone) (PCL) demonstrated that inherently or charge-modified fibers could effectively accumulate charge necessary for flocking [6, 12]. Charge accumulation typically relies on the hydrophilicity of the flock fiber surfaces [13]. To this end, most fibers have a proprietary finish applied to them that allows for rapid charge accumulation. Recently, McCarthy et al. demonstrated that hydrophobic and electrically insulative polymers could accumulate sufficient charge by utilizing conductive fractional fillers following principles of the Percolation Theory [12, 14]. Another method to induce conductivity on a fiber surface may be the implementation of a salt-based system that ionizes under sufficient humidities [15]. It is well known that salt ions hold potential for increasing surface conductivity of objects and in solutions [16,17]. Here, we describe methods for fabricating monofilament microfibers (MFs) from wet spinning (Fig. 1 A) and nanofiber yarns (NFYs) from electrospinning (Fig. 1 B) to create electrostatically flocked scaffolds utilizing a NaCl treatment system (Fig. 1C & D).

One potential use case for electrostatically flocked scaffolds is towards wound healing. Structural anisotropic wound healing scaffolds have shown promise towards accelerating wound healing, promoting angiogenesis, and inducing granulation tissue formation [18,19]. Given the continued fiscal and patient cost of wound treatment, efforts towards advancing wound healing scaffolds towards clinical relevancy persists [20,21]. The high porosity and surface area-to-volume ratio of flocked scaffolds make them appealing wound healing scaffolds as they can allow for nutrient and oxygen circulation within the wound while serving as scaffolds for new tissue formation. To this end, we evaluated the potential use of flocked scaffolds as wound healing treatments in type 2 diabetic mice. In addition to using standalone flocked wound healing scaffolds, we introduced the concept of flock-reinforced elastomers for biomedical applications.

One potential application for flock-reinforced objects is in the production of short fiber-reinforced elastomeric composites [9,22]. Anisotropic composite elastomers may offer an advantage in the treatment of lumbar disc degenerative disease (DDD) [23,24], a pathology in which the breakdown of an intervertebral disc leads to structural instability and chronic pain [25]. The intervertebral disc is located between all vertebral bodies within the spine, excluding C1 and C2 (atlas and axis, respectively), and is identified by the two vertebral bodies in which it separates [26]. The disc is composed of three major structures: the annulus fibrosus, the nucleus pulposus, and cartilaginous endplates [27]. The annulus fibrosus is organized in an alternating, crisscross pattern of type 1 and type 2 collagen strands, varying in angle of orientation, forming an angle-ply structure [27,28]. The collagen matrix produces an anisotropic system designed to withstand vertical compression and fluctuating radial loads, as well as allow for multidirectional torsion [27, 29]. Obstruction of nutrient supply to these cells has been shown to lower oxygen concentration, decrease pH, and impair the ability of the disc to respond and heal from structural strain, highlighting a need to stress-shield the cells within the intervertebral disc [25]. A variety of treatments exist for each stage of the disease progression, yet total disc replacement (TDR) is standard for patients who have failed prior conservative treatment [30]. TDR is preferred in comparison to spinal fusion at the level of the degenerated disc, allowing for restoration of normal disc height and function to alleviate pain without compromising range of motion [31]. Current artificial discs are manufactured with a core of ultra-high molecular weight polyethylene (UHMWPE), a stiff material designed to withstand significant uniaxial compressive forces and resist delamination [32]. Although the stiffness of UHMWPE is desirable from a uniaxial compression standpoint, the material fails to support multiaxial loads or provide shock absorbance for the vertebrae, leading to disc failure at various stress points [28,32]. In an effort to mirror the anatomical organization of an intervertebral disc, we propose utilizing a structure similar to the angle-ply, layered construction of the annulus fibrosus, generated using polydimethylsiloxane (PDMS) polymer composites and electrostatically flocked PCL microfibers.

The aims of this study were to introduce a high-fidelity, easy, and cost-effective method to induce surface charge accumulation on electrically insulative short polymer fibers to achieve high-yield electrostatic flocking. To validate the reproducibility, multi-polymer functionality, and demonstrate the broad biomedical and biomechanical role of electrostatic flocking, three polymer types (PCL, poly(lactic-co-glycolic acid) PGLA, and polylactic acid (PLA)) were used to create standalone NFY and
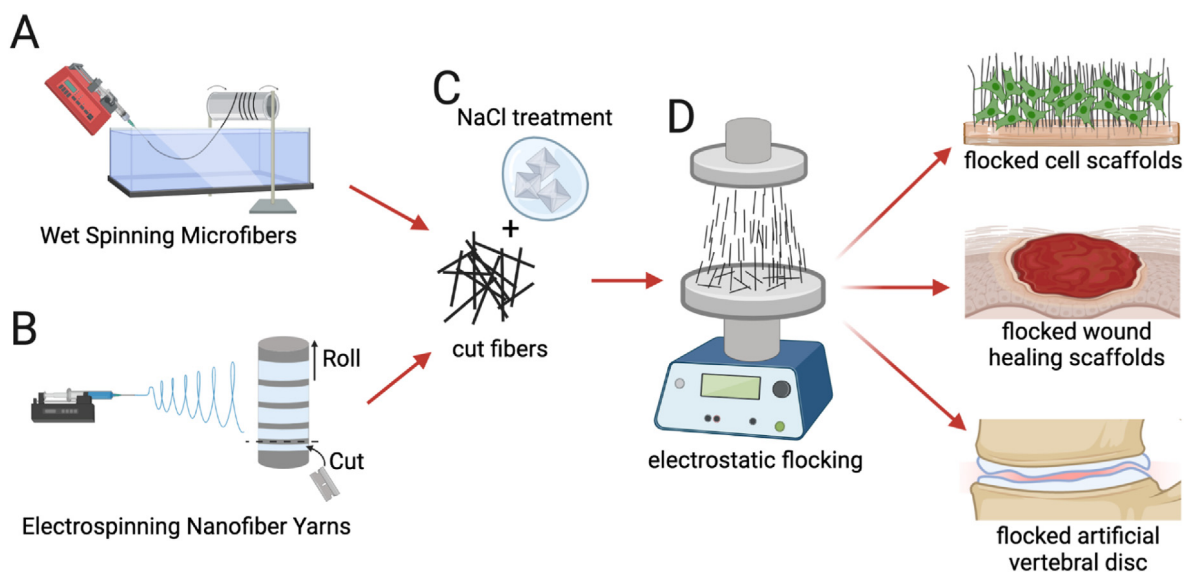

Fig. 1. Schematic illustrating the fabrication of scaffolds by electrostatic flocking for potential biomedical applications. (A) Microfibers fabricated by wet spinning. (B) Electrospun nanofiber yarns fabricated by cutting and rolling. (C) NaCl treatment. (D) Electrostatic flocking and obtained scaffolds for cell growth, wound healing, and artificial vertebral disc replacement.

MF scaffolds, low and high density wound healing constructs, and flock fiber-reinforced artificial vertebral discs (AVDs), respectively (Table 1). The mechanical, biological, and biomechanical effectiveness of flocked scaffolds and AVDs are evaluated herein.

2. Materials and methods

2.1. Production of nanofiber yarns

NFYs were produced by first electrospinning 10% w/v PCL (Mw = 80 kDa, Sigma-Aldrich, St. Louis, MO, USA) dissolved in a 4:1 (v/v) mix of dichloromethane to N, N-dimethylformamide (DCM:DMF) (BDH Chemicals, Dawsonville, GA, USA), based on previous reports [33]. After the polymer solution was homogenous, it was loaded into a 10-cc syringe capped with a blunted 21-gauge needle. The polymer solution was electrospun under ambient conditions (21.6 °C; relative humidity (RH) = 45%) with an applied voltage of 18.0 kV and a flow rate of 0.8 ml/h. During electrospinning, nanofibers were collected on a high-speed rotating drum (7 mm in diameter). After 1 ml of the polymer solution was collected on the drum, the fiber mat was cut into 3–15 mm strips and rolled along the drum to form the NFYs. Using a razor blade, the yarn was cut and removed from the drum.

2.2. Wet spinning of continuous fiber tow

Continuous PCL fibers were prepared with phase-separation wet spinning as previously reported [12]. First, 20% w/v PCL (Mw = 80 kDa, Sigma-Aldrich, St. Louis, MO, USA) and 0.5% w/v F-127 (Sigma-Aldrich, St. Louis, MO, USA) were dissolved in a 4:1 (v/v) mix dichloromethane to N, N-dimethylformamide (DCM: DMF) (BDH Chemicals, Dawsonville, GA, USA) and stirred until a homogeneous solution with uniform viscosity was achieved. Next, a 10-cc syringe capped with a 21-gauge needle was loaded with the polymer solution and extruded under ambient conditions (21.6 °C; RH = 45%) with a coagulation bath of 70% EtOH at a rate of 0.3 ml/h. Fibers were collected on a rotating drum with take-up rates ranging from 5 to 25 RPM. After fibers were collected, they were removed with a razor blade and allowed to air dry. Similarly, PGLA (90:10) (Mw = 60 kDa, DURECT Corporation, Pelham AL, USA) fibers were produced by creating 25% (w/v) PGLA solution dissolved in a 4:1 (v/v) mix of DCM: DMF and extruded under the same conditions as the PCL fibers. In the case of direct extrusion into an NaCl bath, NaCl (0.65 g NaCl/kg ethanol) was added to the bath and the above process was carried out as described.

2.3. Producing NaCl-treated flock fibers

After the MF and NFYs were dried, they were mechanically cut using surgical scissors at approximately 1–2 mm in length. Untreated PLA flock fibers were supplied as pre-cut by Spectro Coating Corp. To separate any fused MF ends, the fibers were plasma treated for 3 min and suspended in an ice water bath. Next, fibers were homogenized in a NaCl-saturated (1.2 g/ml) ice water bath using a probe tip ultrasonicator for 40 min

with a 30 s pulse/10 s rest cycle. It is important to note that separation using sonication methods requires careful maintenance of temperature, depending on the polymer used, as the fibers may fuse together under high heat conditions. Following separation, fibers were collected with vacuum filtration. NFYs did not undergo separating steps but underwent the same plasma and salt wash prior to flocking. The resulting NFYs and MFs were allowed to air dry and were stored at 23 °C and 55% RH until use. All fibers (PCL, PLA, and PGLA) were separated and treated with NaCl as described in this section.

2.4. Electrostatic flocking

Electrostatic flocking generally followed previous studies [12]. In both MF and NFY scaffolds, the adhesive layers served as the substrates. For in vitro and in vivo studies, a 20% w/v gelatin/H$_2$O solution was prepared by dissolving 2 g gelatin in 10 ml of deionized H$_2$O. Similarly, a chitosan (CHS) solution was prepared by dissolving 0.5 g of CHS in 10 ml of 5% w/w acetic acid/H$_2$O. Both solutions were heated at 60 °C until both solutions were homogenous. Then, a 50/50 blend of the CHS and gelatin solutions was created and stored at ambient temperatures until further use. For AVD tests, PDMS was prepared at a 10:1 base: curing agent ratio. In both cases, the adhesive layer was razor coated on the ground electrode such that a thin layer of uniform adhesive remained. MFs and NFYs were removed from humidity-controlled storage (RH = 40%) and MFs (NFYs did not require sieving) were sieved onto the charging electrode with a mechanical sieve (Fig. S3 A). With a distance of 10 cm between each electrode on a MaagFlock SPG 1000 electrostatic flocking machine (Maag Flock GmbH, Mössingen, Germany), an increasing voltage of 30–60 kV was applied until no fibers remained on the charging electrode (Fig. S3 B). Scaffolds prepared with CHS/gelatin adhesives were thermally cured for 5 min at 60 °C and dried at ambient conditions overnight before crosslinking in a glutaraldehyde chamber for 24 h. Scaffolds prepared with PDMS were heat cured at 50 °C for 24 h. Before use, loose fibers were removed with an air hose and scaffolds were incubated in 70% ethanol for at least 24 h to sterilize and remove any remaining loose fibers. Scaffolds used for in vitro and in vivo testing were sterilized using ethylene oxide (EtO) gas sterilization overnight. The use of EtO sterilization and ethanol incubation ensured high sterility while retaining fibrous and anisotropic morphologies.

2.5. Flock yield

Prior to measuring flock yield, fibers were incubated for 24 h at each RH that was tested. RH was controlled in the flocking chamber by using a Hunter 31004 Cool Mist Ultrasonic Humidifier (Hunter Fan Company, Memphis, TN) with deionized H$_2$O and RH readings were taken with a RH meter (Fisherbrand™ Traceable™, Fisher Scientific, Waltham, MA). Flock yield was calculated as the fraction of fibers lifted relative to the number of fibers sieved onto the charging electrode, based on an equation previously reported [10,12].

$$\text{Flock Yield (\% fibers lifted)} = \frac{m_s - m_f}{m_s} \times 100\%$$

Where m_f is the mass of fiber flocked and m_s is the mass of fibers sieved. First, fibers were sieved onto the charging electrode and the mass was taken (m_s). After flocking, the charging electrode was removed again and reweighed (m_f). In most cases, some fibers remained on the surface of the electrode, so it was necessary to take caution during transfer as to not lose fibers to air flow. The difference in masses after flocking was used to calculate the percentage of fibers lifted. While this equation is useful to generally understand flocking yield, one caveat worth mentioning is that the equation does not account for fibers that do not adhere into the adhesive. These fibers may launch into the surrounding flock chamber and would contribute to an overestimation of flock yield.

Table 1
Different scaffold compositions and use cases reported in this study.

Name	Polymer	Fiber Form	Substrate	Application
MF	PCL	microfiber	chitosan/gelatin	in vitro cell scaffold
NFY	PCL	nanofiber yarn	chitosan/gelatin	proof of concept
whMF	90:10 PGLA	microfiber	chitosan/gelatin	in vivo wound healing
avdMF	PLA	microfiber	PDMS	artificial vertebral disc reinforcement

MF: microfiber; NFY: nanofiber yarn; whMF: microfibers for wound healing; avdMF: microfibers for artificial vertebral disc.

2.6. Fiber and scaffold characterization

Fibers and scaffolds were imaged with a scanning electron microscope (FEI Quanta™ 200, FEI Company, Hillsboro, OR, USA), camera (iPhone 8 Plus, Apple, Palo Alto, CA, USA), or USB microscope (AmScope, Irvine, CA, USA). Length measurements were taken using NIH ImageJ's measure analysis tool, with pixels calibrated to each measurement scale bar. Similarly, fiber diameters were measured using open-source ImageJ plugins SkeletonJ and DiameterJ. First, SEM images of each fiber were taken. SkeletonJ was used to create skeleton images with which DiameterJ used to estimate mean diameters with [7]. Scaffold fiber orientation was calculated by analyzing SEM images with the ImageJ plugin OrientationJ, which uses tensor analysis to quantify mean orientations of the image field [34]. Compression resistance of PCL NFY and MF scaffolds were conducted on a CellScale UniVert (CellScale, Ontario, CA) utilizing a 200 N loadframe. Four cyclic compressions to 50% were conducted under ambient conditions with 10 s between each compressive load. Abrasion resistance was measured using a modified and standardized thumb (rub) test, which is a flocking industry standard [8,12]. A plastic, round-edged stir bar was placed horizontally over the flocked surface and rubbed back-and-forth with a consistently applied pressure. After each set number of abrasive cycles, the mass of the flocked sample was taken and a change in mass was calculated.

2.7. Anatomically accurate L4-L5 model preparation

Anatomically accurate L4 and L5 vertebrae were created using additive manufacturing. First, de-identified computed tomography (CT) scans of human L4 and L5 vertebrae were accessed via an open-access website, Thingiverse™, as STL file types (Fig. S9 A-D). The STL files were originally supplied by the BodyParts3D database under a creative commons attribution. Next, the STL files were transferred to a LulzBot Mini v2.0 (Fargo Additive Manufacturing Equipment 3D, LLC, Fargo, ND, USA) for 3D printing. Models were printed using 3 mm diameter poly lactide (PLA) filament (MatterHackers Inc, Lake Forest, CA, USA) at 50% infill density at a 40 mm/s rate, with a wall thickness of 1 mm. Printing was conducted with a nozzle temperature of 220 °C and a build plate temperature of 70 °C. A support was generated for stability during the printing process. After printing, support material was removed, and the vertebrae were used for disc preparation (Fig. S9 E). All printing values are listed in Table S1.

2.8. Creating artificial discs

To create AVDs, round molds (diameter = 55 mm, height = 8 mm) were 3D printed using the above-mentioned parameters and materials. For control discs (no fiber reinforcement), 11 ml of 10:1 elastomer base: curing agent polydimethylsiloxane (PDMS) (Sylgard™ 184 Silicone, Dow Corning, Midland, MI, USA) was poured into the mold and cured in at 65 °C over for 24 h to reach a final disc height of 7 mm. PDMS was used as a model elastomer due to its low cost, mechanical robustness, ease of use, and lengthy history in biomedical applications, particularly as a component in lumbar disc replacements [35,36]. After removal from the mold, the PDMS discs were die-cut using a custom cut mold based to fit between the L4 and L5 vertebrae (Fig. S9 F–H). To create the fiber-reinforced discs, a small amount of PDMS was knife-coated on the ground electrostatic flocking electrode. A monolayer of NaCl/PLA fibers (Fig. S8A-B) (diameter = 20 μm, length = 0.5 mm) was sieved onto the charging electrode and flocked upwards towards the PDMS layer for 1 min with the applied voltage gradually increasing from 30 kV to 60 kV. After flocking, the ground electrode was removed and allowed to cure (Fig. S8 C). The flocked PDMS was cut to fit into the PDMS mold and enough PDMS was added to barely cover the top of the fibers. This was repeated until the final height of the disc was ~8 mm, which is within the range for L4-L5 thickness reported in both males and females [37,38]. Fiber-reinforced discs were die-cut using the same anatomical shape as

the control discs. Fidelity of fit was checked by positioning the AVD between the 1:1 L4 and L5 replicate vertebrae (Fig. S9 G & H).

2.9. Compression testing

Quasi-static compression tests of control, isotropic, and flocked AVDs were conducted on a uniaxial servo-hydraulic 810 material test system (MTS) employing a 25 kN loadframe which was calibrated by Instron (Instron, Norwood, MA, USA). Load and displacement data for each AVD group were collected from the load frame and communicated through an 8800 minitower controller. The controller contains sensor conditioning cards for the system transducers and transfers data between the transducers and the computer. The controller also communicates with the load frame via a frame interface board (FIB) inside the load frame. The FIB links all the electrical components of the frame together. Stress relaxation and dynamic tests were performed on the AVDs to delineate differential mechanical properties. Subsequently, dynamic testing was performed at the end of a stress relaxation; this allows the sample material to be at equilibrium. In this experiment, the discs with an area of 1620 mm^2, were compressed to 20% strain for 180 s, relaxed for 600 s, and subjected to cyclic strain. Cyclic testing was conducted at a 1 Hz with a 2% strain amplitude for 100 cycles. Each experiment was repeated three times and similar results were gathered at room temperature (25 °C) and under ambient conditions. Aggregate data was collected and stored for further analysis. In most cases, AVDs returned to their original shapes after all compression tests. One sample from the flocked AVDs had minor delamination of a layer following compression cycles.

2.10. Model protein release and absorption ratios

Absorption ratio was determined by taking the initial dry mass (m_i) of NFY and MFs. After 24 h of immersion in 1 ml of a phosphate buffered saline (PBS)/bovine serum albumin (BSA) (500 μg/ml), fibers were removed, lightly compressed to exude excess liquid, and weighed for a final wet mass (m_f). A percent change in mass was calculated with the following equation:

$$Mass\ Change = (\frac{(m_f - m_i)}{m_i}) \times 100\%$$

Protein release was determined using BSA as a model protein and quantified with a BCA assay (Pierce BCA Protein Assay Kit, Thermoscientific, Rockford, IL, USA). First, nine different dilutions for a standard curve using PBS (diluent) and BSA (stock) were prepared. Triplicates of approximately 0.2 g of NFYs and MFs were immersed in 1 ml of 500 μg/ml BSA in PBS and incubated at (37 °C) overnight. The following day, samples were moved into 1 ml of fresh PBS. After 5 min, 10 min, 15 min, 30 min, 1 h, 2 h, 4 h, 12 h, and 24 h, 25 μl of the solution was removed and transferred into a 96 well plate. At the endpoint of the study, a mixture of BCA Assay working reagent was added and absorbance was measured at 540 nm using a plate reader (BioTek Synergy H2 Hybrid Reader, BioTek Instruments, Winooski, VT, USA). Absorbance was correlated to BSA concentration using a standard curve established during reading.

2.11. Cell study

Prior to cell studies, salt-treated PCL MFs and chitosan/gelatin flocked scaffolds were fabricated, excised with an 8-mm biopsy punch, and sterilized with EtO gas sterilization for 24 h. After gas sterilization, scaffolds were vigorously agitated in 70% ethanol for 24 h to remove any loose fibers. Before seeding, scaffolds were immersed in completed DMEM. HaCaT cells were seeded at 10000 cells/scaffold and cultured for 7 days. At 3, 5, and 7 days, cells were stained with LIVE/DEAD™ staining kit and imaged using a confocal laser scanning microscope (Zeiss 710 Confocal Laser Scanning Microscope, Zeiss, Dublin, CA). Z-stack images

were taken and used to construct both 3D and depth mapping renderings on Zeiss' Zen Blue software (Zeiss, Dublin, CA). Depth values are automatically generated by Zeiss' software and are presented unaltered. Viability was calculated as the fraction of live cells/total cells. After confocal images were acquired following live/dead staining, images were split by color (green and red) and cells expressing each color were counted using ImageJ's cell counter plugin. Normalized fluorescence was measured by reading the integrated density of the image and subtracting background fluorescence on ImageJ, as reported in previous studies [39]. Cell migration was measured by taking length measurements from the depth of cells along the Z axis, resulting in a 3D length map of the imaged field.

2.12. Animal study

All portions of this animal study were conducted following approval from the University of Nebraska Medical Center's IACUC in accordance with animal protocol #19-069-07-FC. Ten-week old B6·BKS(D)-Leprdb/J male diabetic mice were purchased from Jackson Laboratory (Bar Harbor, ME) and were fed, housed, operated on, and cared for in-house at the University of Nebraska Medical Center. Two scaffolds were created: low-density (LF) and high-density (HF) flocked scaffolds consisting of PGLA (90:10) fibers (~1 mm in length) and a 50/50 CHS/gelatin substrate/adhesive. Scaffolds were punched into 8 mm diameter scaffolds, washed with EtOH to remove loose fibers, and gas sterilized with ethylene oxide. Mice were anesthetized under 4% isoflurane in oxygen for roughly 5 min while on a heating pad. Diabetic status was ensured by taking blood glucose readings of each mouse. Each mouse was shaved and treated with buprenorphine SR (0.5–1 mg/kg body mass) injected subcutaneously. The surgical site was sterilized and treated thrice with povidone-iodine and EtOH wipes. During surgery, mice were maintained at 2% isoflurane. Two circular defects were made using a 8 mm sterile biopsy punch (Integra LifeSciences, Plainsboro Township, NJ), and a 10 mm inner diameter silicone wound splint was glued and sutured into place with silicone bonding adhesive and sutures (Fig. 7 A). Splints were used to prevent dermal contraction, as several studies indicate the use of splinted wounds increases the mouse-to-human crossover [40]. For treatment groups, each scaffold was directly inserted into the wound with the fibers entering the wound bed. Tegaderm was applied over each wound and post-operative monitoring for 30 min was conducted. Each group (LF, HF, negative control (no treatment)) had four mice with 2 wounds each. Two time points, 7 and 14 days, were used. Mice were housed for 7 and 14 days and at each time point 2 mice from each group were euthanized using CO_2 and bilateral thoracotomy. Explants of the wound and surrounding tissue were taken from each wound site and submerged in formalin for 1 week before undergoing hematoxylin and eosin (H&E) and Masson's trichrome staining (TRI) at the University of Nebraska Medical Center's in-house tissue science facility. Histology images were analyzed, and the most representative images were presented. Re-epithelialization was measured as the percent of new epithelial layer over the wound area. Angiogenesis was measured as the number of vessels/mm^2 and vessels were identified with two criteria: 1) presence of endothelial lining and 2) presence of erythrocytes. To measure granulation tissue formation, collagen deposition was indirectly measured using integrated density (the sum of the values of the pixels within the region of interest (ROI)) following previous studies [41]. Briefly, slides stained with TRI were opened in ImageJ. Within the wound area (defined within the 8 mm defect size), images underwent color deconvolution. Green color channels omit stained cellular nuclei and retain collagen. The integrated density was subsequently measured within each ROI (integrated density = ROI area x mean gray value).

2.13. Statistical analysis

Other than the cyclic compressive data for AVDs, all data is expressed as the mean ± standard deviation and a minimum of 3 samples were used

in each experiment. Mechanical data from AVD testing was expressed as median values. For pairwise columnar comparisons, ordinary one-way ANOVA with Tukey's multiple comparisons post hoc testing were performed. For grouped analyses, 2-way ANOVA with Tukey's multiple comparisons post hoc testing was performed. Curve fitting followed GraphPad Prism's curve fitting guide. Line plots (e.g., stress-strain, force-strain, and distribution) curves underwent 10% smoothing. All measurements taken on SEM or photograph images used calibrated length measurements. Statistical significance was expressed as *p < 0.05, **p < 0.01, ***p < 0.001, ****p < 0.0001, and a lack of pairwise comparison bars implies a lack of significance (p > 0.05). Figures are all original and were created using BioRender and Microsoft PowerPoint. All statistical analyses were performed using GraphPad Prism 9 for macOS (version 9.1.1).

3. Results and discussion

3.1. MFs and NFYs make size-tunable flock fibers with distinct functional properties

Previous studies demonstrated the role of fiber morphologies and topographies on modulating cell migration rates and lineage differentiation [6,11]. The ability to tune the size and topography of fibers for tissue engineering applications offers a variety of increased tunability, particularly in cases where it may be favorable to adjust the fiber surface area to increase or decrease the migratory rate of localized cells [42]. To this end, PCL MFs produced from wet spinning were tuned and standardized with a best-fit trend line. The diameters of the fibers were adjusted by increasing the rotations per minute (RPM) of the take-up drum during wet spinning. As take-up rate increased, the average fiber diameter decreased. At 5, 10, 15, 20, and 25 RPMs, PCL fiber diameters were 33.45 ± 0.65, 20.74 ± 0.24, 18.07 ± 0.44, 15.10 ± 1.3, and 12.11 ± 0.72 μm, respectively (Fig. 2A–C). Diameters varied significantly at each 5 RPM interval change (P < 0.0001, n = 100). Similarly, NFYs prepared from twisting electrospun nanofiber have easily-controlled diameters which are determined by the initial width and thickness of the nanofiber mat [43]. Nanofiber mats approximately 30 μm thick were cut into 3, 6, 9, 12, and 15 mm strips and consisted of semi-aligned nanofibers as confirmed via SEM imaging (Fig. S2 A & B). Most nanofibers diameters ranged from 500 nm to 1 μm. The nanofiber strips were rolled along the length of the collection drum to form NFYs (Fig. S2 C&D). As anticipated, thinner strips resulted in NFYs with smaller diameters. Strips 3, 6, 9, 12, and 15 mm in width resulted in NFYs with 161.5 ± 24.70, 295.8 ± 15.59, 583.40 ± 35.50, 848.8 ± 6.237, 1195 ± 8.854 μm in diameter (P < 0.0001, n = 100).

Due to their dramatically different bulk and surface properties, MFs and NFYs vary in functionality and mechanical stability. To demonstrate how each type of fiber has distinct properties, a series of mechanical tests and protein absorption/release studies were conducted. An equivalent mass (2 mg) of MFs and NFYs were totally submerged in a BSA solution (500 μg/ml) for 10 min and their absorptive properties were evaluated. NFYs absorbed significantly more (276.00 ± 35.29)% of their mass than MFs (179.40 ± 42.08)% (P = 0.0382, n = 6) (Fig. 3 A). Similarly, a BSA release assay was carried out after allowing each fiber type to reach maximum saturation. Protein elution was measured by incubating 2 mg of each BSA-saturated fiber in 37 °C PBS solution for 12 h. At every collection time point (1, 5, 10, 15, 30, 60, 120, 240, and 720 min), NFYs released significantly more protein than the equivalent mass of MFs (Fig. 3 B). Additionally, after 60 min, MFs had no significant increase in BSA release, while NFYs had continued significant BSA release up to 240 h. By the conclusion of the BSA release assay, NFYs achieved a total BSA concentration of nearly 400 μg/ml, while MFs achieved just under 100 μg/ml. Fundamental differences in fiber morphologies (i.e., NFYs have microporous surface properties while MFs are smooth and solid) dictate their absorption and release abilities, a phenomenon which is well documented in previous studies investigating the drug release properties
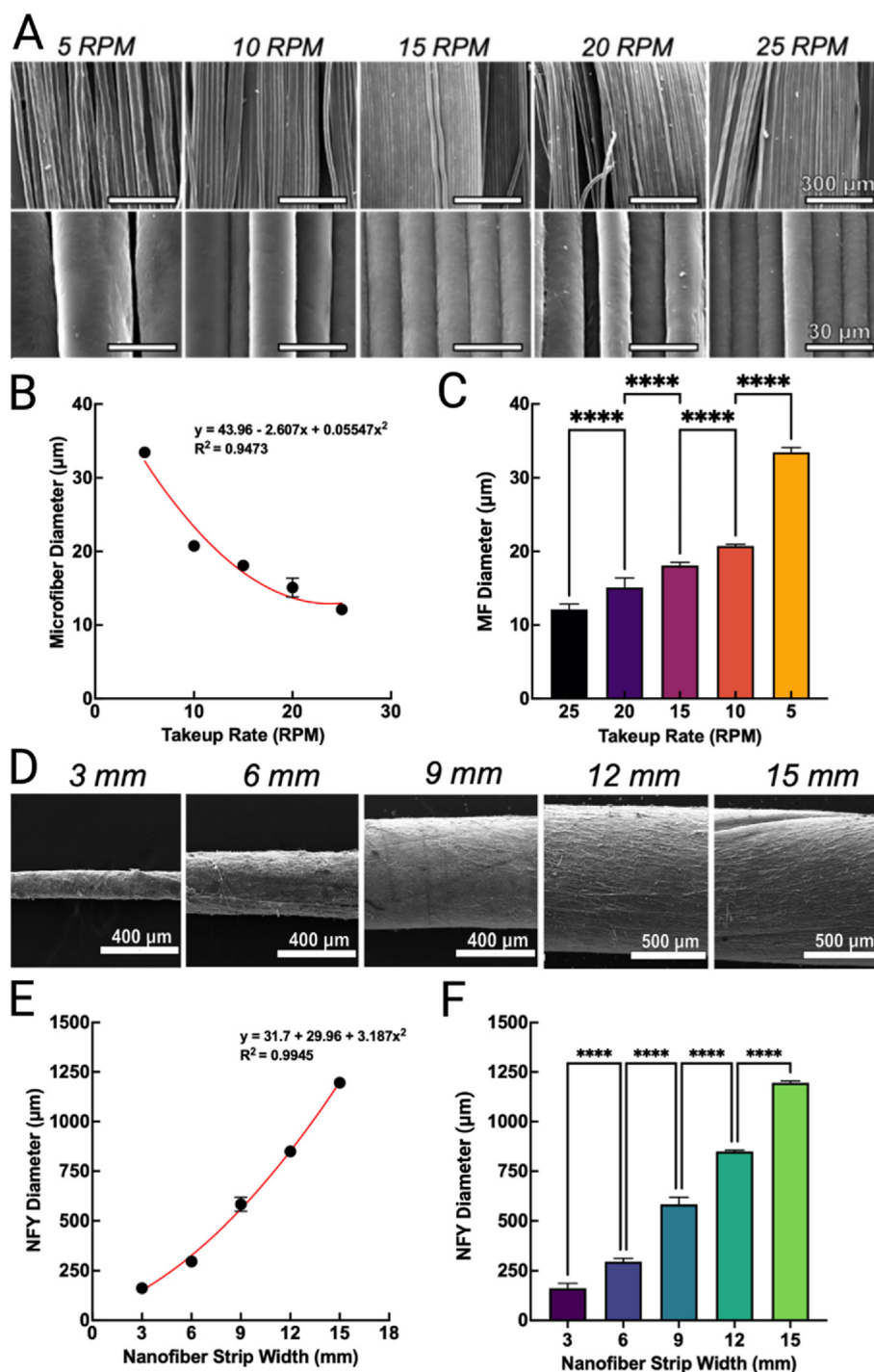
Fig. 2. Optimization of fiber fabrication. (A) SEM images of PCL microfibers prepared at increased take-up rates. (B) Curve-fit for microfiber diameter estimation for wet spinning. (C) Comparison of average microfiber diameters. (D) SEM images of nanofiber yarns rolled from different diameter nanofiber strips. (E) Curve-fit guide for nanofiber yarn diameter estimation. (F) Comparison of average nanofiber yarn diameters. NFY: nanofiber yarns.

of NFYs [44,45]. MFs rely upon adsorption (surface attraction) to hold and release compounds, while NFYs can absorb solutions between and within their nanofibrous pores [46]. The degree to which NFYs are spun and their original nanofiber composition can be used to tune their release profiles, whereas MFs are limited to their bulk composition and morphology.

In addition to having distinct absorption and release profiles enabled by differences in morphological features, MFs and NFYs exhibit different mechanical properties as well. For mechanical tests, MFs and NFYs with average diameters 33.45 μm and 161.5 μm were subjected to tensile testing. Not surprisingly, monofilament MFs exhibited higher elasticity, reaching a maximum strain of (217.00 ± 21.98)%, but a lower break force averaging 0.07 ± 0.022 N. Conversely, NFYs had a significantly lower max strain of (89.95 ± 21.38)%, but a higher break force of 9.267 ± 1.87 N ($P = 0.002$ and $P = 0.001$, respectively, $n = 3$) (Fig. 3C & D). Fiber diameter and bulk morphological composition undoubtedly have large roles in modulating mechanical features of the fibers. In this case, NFYs are stronger than MFs due to their larger size and nanofibrous multifilament composition [47], though they are not as elastic as they resist fiber necking more than MFs [48]. Other studies have examined
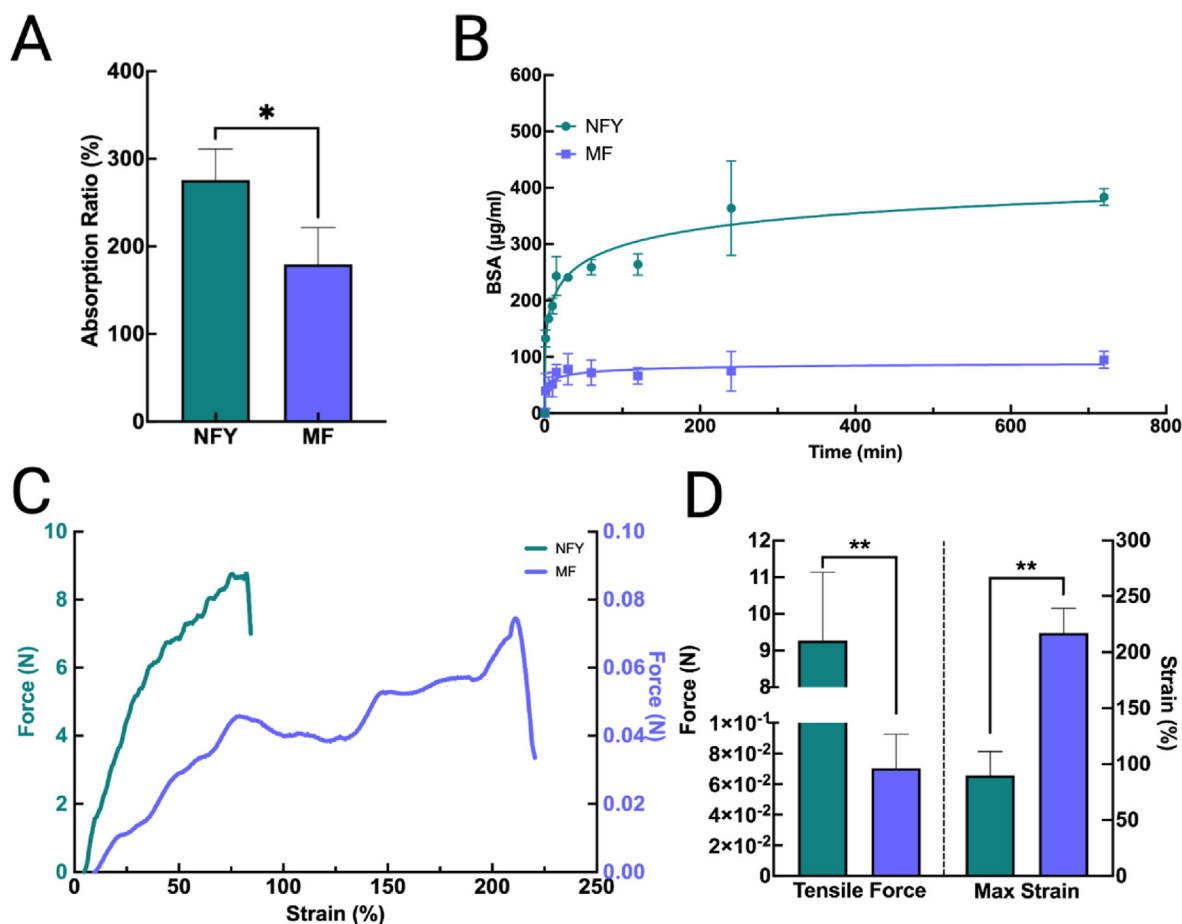
Fig. 3. Characterization of microfibers and nanofiber yarns. (A) Absorption ratios of each fiber type after immersion in a BSA solution. (B) BSA release profiles of each fiber type. (C) Force-displacement curves of each fiber type. (D) Maximum break forces and maximum strains of each fiber type. NFY: nanofiber yarns. MF: microfibers.

crystallinity and polymer chain orientation as primary drivers behind mechanical strength of fibers [49]. Though the NFYs and MFs have different cross-sectional surface areas, we hypothesize that the multifilament and twisted nanofibers within the NFYs do not allow for as much linear displacement and impart the majority of the tensile strength noted.

3.2. Reversible incorporation of NaCl improves flock yields

To create surfaces capable of accumulating sufficient charge for flocking, a novel method utilizing NaCl (salt) was developed. The rationale behind using NaCl as an ionizable salt-based surface treatment was based on its in situ tolerability at modest concentrations, ease of use, low cost, and removability [17,50–52]. During hydration, NaCl crystals dissociate into their ionic forms Na^+ and Cl^-. The incorporation of ionic liquids onto the surface of the fibers allows charge accumulation to occur and a charge differential is maintained until a sufficient Coulombic force lifts the fibers towards the ground electrode [53,54]. To this end, two methods for incorporating salt onto MFs were tested for efficiency at RH = 40%. In one case, fine salt was directly added to the polymer solution prior to wet spinning or electrospinning and, in the other case, a saturated salt solution was used during the final rinse of the fibers before flocking. The presence of salt was confirmed via SEM, in which salt crystals appeared on the surface of both MFs and NFYs (Fig. 4 A & C). The salt crystals could be easily removed by agitating the flocked scaffolds in a water bath for several seconds, which was confirmed by SEM following a water rinse (Fig. 4 B & D). To evaluate which salt incorporation technique resulted in the highest flocking yield, a known mass of MFs from each method were flocked. Similar to previous reports [12], MFs with salt directly added during fabrication had an average flock yield of (53.33 ±

6.02)%, MFs with a salt wash prior to flocking had an average flock yield of (79.17 ± 7.30)%, and untreated MFs had an average yield of (21.82 ± 4.12)% ($P < 0.0001$, $n = 6$) (Fig. 4 E).

After determining whether a salt wash prior to flocking resulted in the highest yield, we sought to elucidate the effect of RH on flock yield. MFs and NFYs with and without salt treatment were flocked at different RHs. As previously mentioned, hydration on the fiber surfaces is necessary for ionization of the NaCl crystals to occur. A fine interplay between ionizing the surface of the fibers and weighing them down with overhydration exists. We optimized this system by flocking salt-treated MFs and NFYs at different RH. Salt-treated MFs achieved a maximum flock yield of (91.67 ± 4.04)% at RH = 40%, while untreated MFs achieved a maximum flock yield of (50.33 ± 5.13)% at RH = 50%. From RH 60–70%, fibers experienced a decrease in flock yield. Between RH 10–50, salt-treated MFs had significantly higher flock yields compared to untreated MFs ($P </= $(0.0001–0.0214), $n = 3$) (Fig. 4 F). Similarly, NFYs achieved a maximum flock yield of (72.09 ± 7.64)% at RH = 40%, while untreated NFYs achieved a maximum flock yield of only (41.42 ± 9.10)% ($P < 0.0001$, n = 3). With increasing RH, NFYs experienced a more rapid decrease in flock yield, likely due to their ability to absorb water, and thus increasing their mass. All yields and ANOVA comparisons are reported in Fig. S4 and flock yields of each fiber type at each RH are shown in Table 2. Increasing mass necessitates a stronger Coulombic force for flocking, and salt ionization on the surface of NFYs is limited to mostly their surface. Therefore, achieving a RH that facilitates total surface wetting is necessary for uniform charge accumulation. Despite their significantly larger size and mass, one advantage NFYs have over MF during flocking is their reduction in fiber-fiber interactions. After sieving MFs, it is common to have some fibers adhere to one another, particularly at higher RHs. This
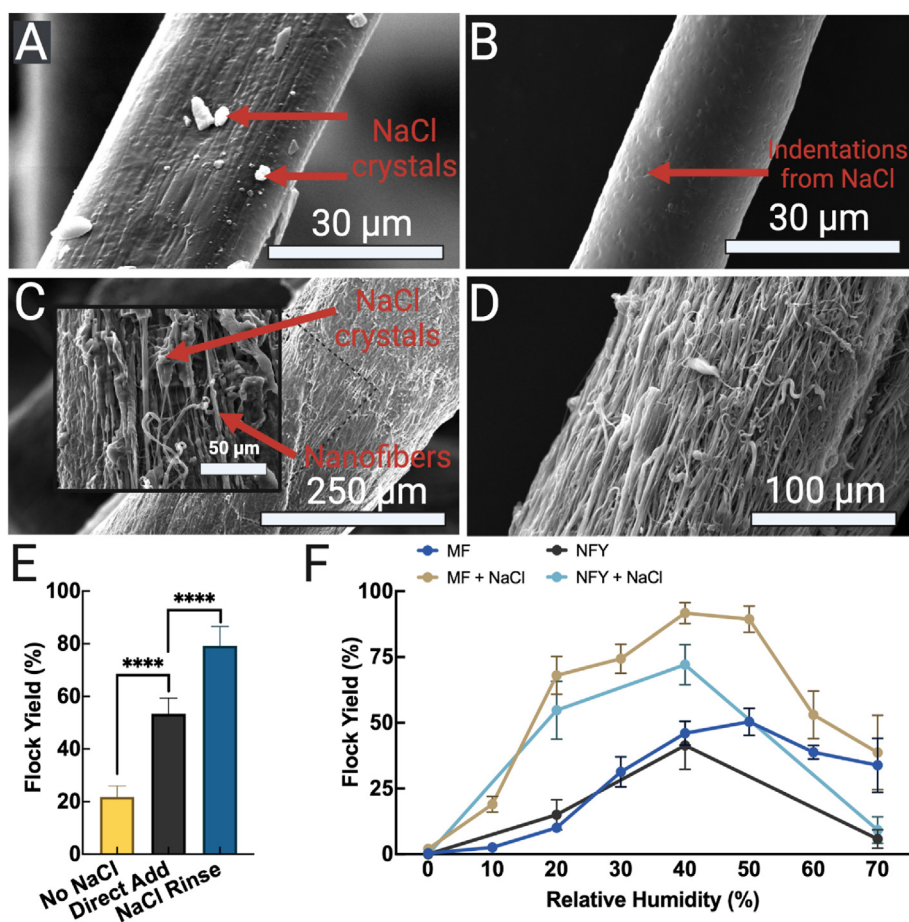
Fig. 4. Introduction of salt via salt bath washing increases flocking yields over a range of relative humidity. (A) SEM image of a salt-covered (red arrows) microfiber (MF) after flocking. (B) SEM image of a flock fiber after washing with H_2O. (C) SEM of a salt-covered nanofiber yarn (NFY) after flocking and (D) after rinsing with H_2O. (E) The flock yield of MFs prepared with two different salt implementing strategies and (F) the resulting yield of NaCl-rinsed and untreated MFs and NFYs at a range of humidities.

Table 2
Flocking yields at different relative humidities.

Relative Humidity (%)	MF	MF + NaCl	NFY	NFY + NaCl
0	0.33 ± 0.58	2.00 ± 0.99	0.00 ± 0.00	0.00 ± 0.00
10	2.57 ± 0.91	19.01 ± 3.00		
20	10.10 ± 1.72	68.00 ± 7.21	15.03 ± 5.78	54.77 ± 11.02
30	31.30 ± 5.7	74.33 ± 5.50		
40	46.00 ± 4.58	91.67 ± 4.04	41.42 ± 9.10	72.09 ± 7.64
50	50.33 ± 5.13	89.33 ± 5.03		
60	38.79 ± 2.57	53.00 ± 9.00		
70	33.87 ± 10.28	38.67 ± 14.19	5.78 ± 3.54	9.22 ± 5.10

MF: microfiber; MF + NaCl: microfiber treated with NaCl; NFY: nanofiber yarn; NFY + NaCl: nanofiber yarn treated with NaCl.

phenomenon is common and tends to increase with decreasing fiber size [8]. During flight, these fiber aggregates can interfere with flock uniformity and yield and are referred to as clouding. Nevertheless, in both cases, MFs and NFYs exhibited an increased flocking yield after a salt treatment and suffered from decreased flock yields at high RHs. These findings are consistent with those previously reported [12,15]. Based on these findings, fibers should be stored and flocked between RH 20–50%. After scaffolds are cured, it is important to remove the salt on the surface of the fibers, as high concentrations of salt may induce local apoptosis by increasing the expression of heat shock protein 60 (HSP60) [55]. Further

investigations into the flocking effects of different salt concentrations should be considered, as elucidating the synergistic role of salt treatment and relative humidity is yet to be fully understood.

3.3. Characterization of flocked microfiber and nanofiber yarn scaffolds

Many previous reports have looked into the characterization and optimization of electrostatically flocked scaffolds. Some of the main findings in these studies are that: 1) fiber density and thus porosity is mainly modulated by flock time (i.e., how long voltage is applied) and fiber amount sieved (but not fiber length) [11]; 2) scaffolds with shorter fibers and higher fiber densities have higher compressive moduli [10, 11]; and 3) CHS, gelatin, and CHS/gelatin adhesive/substrates are mechanically suitable for in situ and in vivo applications [5,6,12]. To emulate some of the favorable previously reported metrics, similar protocols were used to create flocked MF and NFY scaffolds. Both MFs and NFYs ranged in length from 1 to 2.2 mm in length, as verified by SEM imaging in Fig. 5 A & C. Flocked scaffolds consisting of MFs demonstrated a velvety appearance, while scaffolds composed of NFYs appeared to be more sparsely populated (Fig. 5 B & D). Orientation analysis comparing MFs, NFYs, and rayon (industry control) showed that rayon fibers had the highest degree of alignment, though MF scaffolds had similar orientation distributions (Fig. 5 E). NFYs had relatively broad distribution peaks, in part due to the dramatic size variation and relative impact on colorimetric tensor measurement. Abrasion resistance revealed that MF scaffolds lost less than 5% of their mass after 500 abrasive cycles, while NFY scaffolds lost nearly 100% by 250 cycles (Fig. 5 F). Due to the dogbone shaped ends on the NFYs, it is reasonable to assume the amount of NFYs embedding into the adhesive layer is less than that of MFs. In addition, NFYs have larger surface area and lower elasticity so they resist abrasion
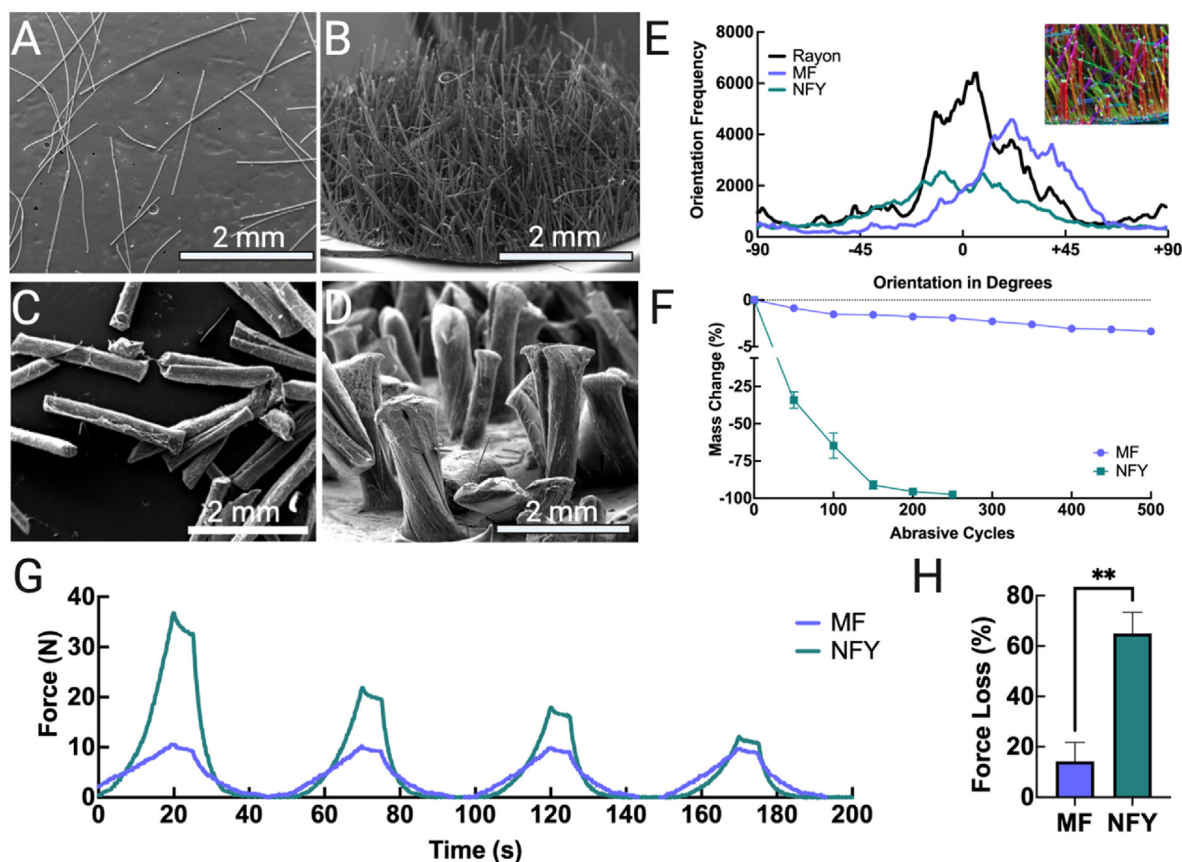
Fig. 5. Flock fibers and scaffold characterization. (A) SEM images of microfibers (MFs) and (B) flocked MF scaffolds. (C) SEM images of nanofiber yarns (NFYs) and (D) flocked NFY scaffolds. (E) Anisotropy measurements of rayon (control), MFs, and NFYs (colored image shows the tensor analysis of MF scaffolds used to plot orientation curves. (F) Mass loss from abrasive cycles of MFs and NFYs during rub testing. (G) Compression curves of NFY and MF scaffolds undergoing 50% displacement and (H) average compressive force lost between the first and fourth compressive cycle.

more than MFs, resulting in a faster mass loss during abrasive cycles. Evaluation of compressive strength of MF and NFY scaffolds showed distinctly different compression curves. After 4 cycles of 50% displacement, compression curves were normalized and compared (Fig. 5 G). Notably, NFYs had a 3-fold higher max compression resistance (36.95 N) during the first compressive load compared to MF scaffolds (10.66 N). However, the compression resistance decreased significantly between the successive loading periods, due to the permanent deformation caused by NFYs being flattened. Unlike the NFY scaffolds, MF scaffolds had little change in compression resistance between the first and last compression. The force change between the fourth and first load was calculated for each scaffold and expressed as a percent loss. NFY scaffolds lost $(64.95 \pm 8.42)\%$ of their maximum compressive load, while MF scaffolds lost only $(14.26 \pm 7.51)\%$ ($P = 0.0015$, $n = 3$) (Fig. 5H). Based on these results, MF scaffolds were used for the remaining in vitro and in vivo studies, though further investigations into optimizing the mechanical properties of NFY scaffolds may warrant their in vitro and in vivo applications in the future.

3.4. Flocked scaffolds sustain and modulate cellular proliferation

On their own, flocked scaffolds have demonstrated the ability to modulate cell migration, sustain tissue formation, and facilitate cell differentiation [6,12]. Confocal images including brightfield reveal densely populated scaffolds at days 3, 5, and 7 (Fig. 6 A). By day 7, HaCaTs appeared to form larger cell aggregates, presumably along fibers. 3D

mapping of the cells allows for spatial orientation to be observed as well as confirmation that fibers retain anisotropy under culture conditions (Fig. S5). It is worth noting that the fibers retain alignment under culture conditions, but that this is largely due to how well the fibers embed into the adhesive and how inherently rigid the fibers are. To this end, cells appeared relatively homogeneously distributed along the scaffold fibers, as observed in Fig. 6 B. To quantify the cell migration, the height of cells along fibers were quantified with colorimetric depth mapping (Fig. 6C). Analysis of the Live/Dead, 3D Live/Dead distribution, and depth mapping images revealed several key findings. First, color channel splitting of LIVE/DEAD staining (e.g., red, and green channels) revealed excellent viability over the 7-day culture period, with days 3, 5, and 7 achieving viabilities of $(99.7 \pm 0.58)\%$, $(98.00 \pm 0.97)\%$, and $(95.67 \pm 0.61)\%$, respectively (Fig. 6 D) ($P = 0.0754$, $n = 3$). Given that a relatively high density of cells was seeded, we suspect the slight decrease in viability is a result from cells detaching after reaching confluency. Similarly, the normalized fluorescence intensity of the 3D Live/Dead, measured as normalized integrated density throughout the entirety of the scaffold volume, revealed a steady increase in intensity throughout the 7-day culture, though large local deviations in 3D intensity were noted where cells did not occupy the scaffold (Fig. 6 E) ($P = 0.6244$, $n = 3$). Finally, spatial analysis from depth mapping revealed significant migration was achieved at each time interval, with cells traveling an average of 103.20 ± 18.27 μm, 181.11 ± 27.33 μm, and 427.10 ± 22.75 μm at day 3, 5, and 7, respectively (Fig. 6 F) ($P < 0.0001$, $n = 3$).
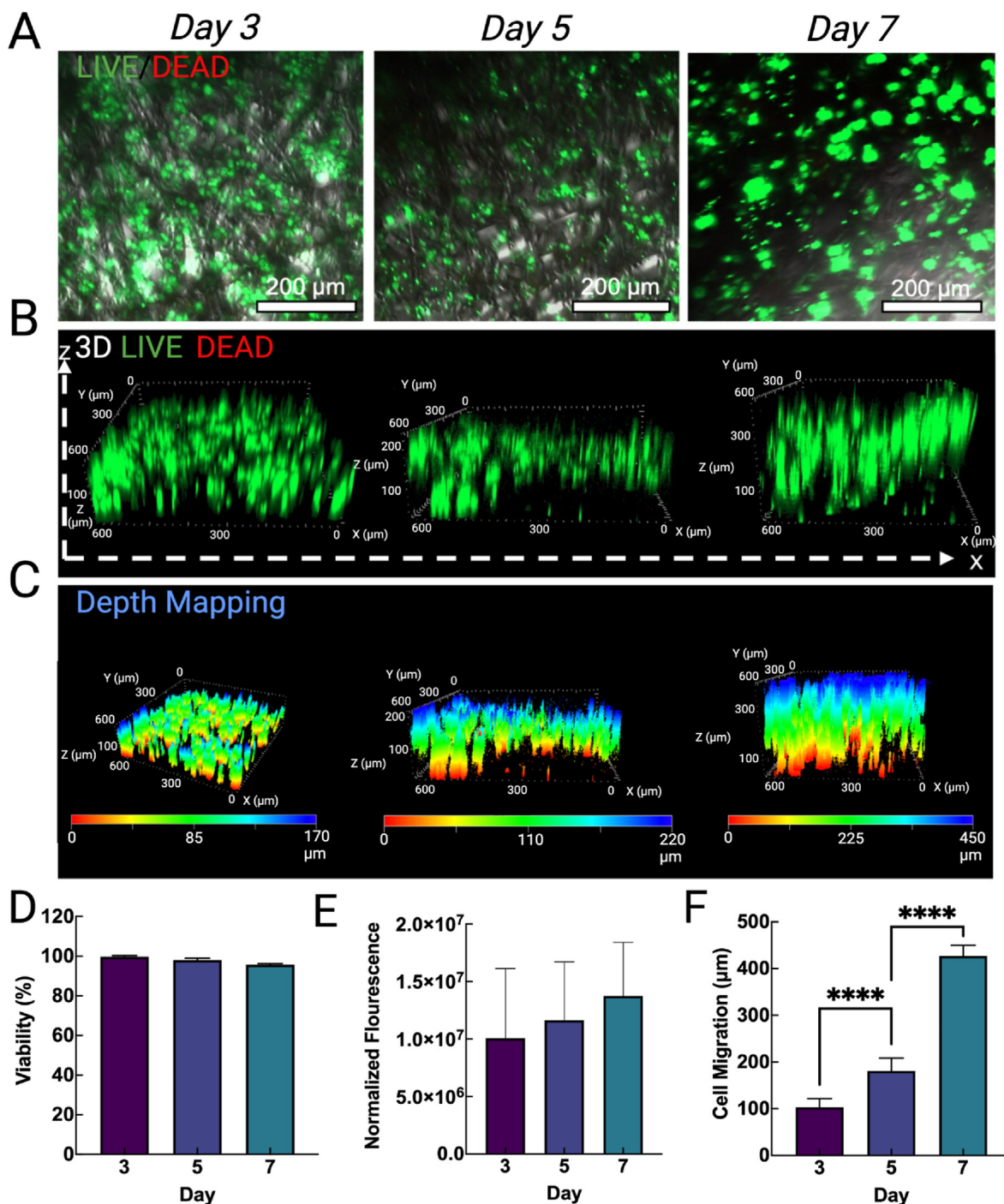
Fig. 6. HaCaT proliferation and migration. (A) Live/Dead + DIC confocal images of HaCaT cells cultured on salt-treated PCL MF flocked scaffolds for 3, 5, and 7 days. (B) Normalized viability over the 7-day culture period. (C) 3D Live/Dead images showing cell distribution throughout the flocked scaffolds. (D) Normalized fluorescence intensity of HaCaT-seeded scaffolds at 3, 5, and 7 days. (E) Depth mapping of HaCaTs on the flocked scaffolds at 3, 5, and 7 days and (F) their related leading average cell migration measurements.

3.5. Flocked scaffolds show a fiber density-dependent wound healing effect

To evaluate the wound healing capacity of rapidly-degrading flocked PGLA (90:10) fiber scaffolds with CHS/gelatin adhesive as substrate, scaffolds were placed directly in contact with 8 mm induced full thickness wounds in type II diabetic mice and observed for 7 and 14 days. Scaffolds were positioned with fibers penetrating into the wound bed such that the substrate was near flush with the epidermis on the wound

edge (Fig. 7 A & B). Several metrics were measured as wound healing hallmarks following histological analysis of H&E and TRI staining at day 7 and 14 post-implantation (Fig. 7C & D). Re-epithelialization (Fig. S6 A; red arrows), measured as the percent of the original defect that was re-epithelialized by day 7 and 14, showed a fiber-dependent, wound healing effect. By day 7, mice without treatment reached $(41.53 \pm 11.43)\%$, while those with low-density and high-density flocked scaffolds reached $(52.37 \pm 18.90)\%$ and $(68.00 \pm 4.88)\%$, respectively ($P = 0.013$, $n = 2$)

(Fig. 7 E). Similarly, after 14 days, mice without treatment reached an average re-epithelialization of $(59.40 \pm 12.07)\%$, and those with low-density and high-density flocked fibers reached $(72.30 \pm 7.7)\%$ and $(83.02 \pm 10.50)\%$, respectively ($P = 0.0277$, $n = 2$) (Fig. 7 E). The positive relationship between high fiber density and increased cell infiltration was established in a previous study, which investigated host cell infiltration into a subcutaneously implanted flocked scaffold [12]. In addition to modulating re-epithelialization, blood vessels (Fig. S6 A; black arrows) within the region of interest (the wound edges and within the defect area) were quantified for each treatment group at each time-point. Vessel counts at day 7 were 0.58 ± 0.24, 1.64 ± 0.92, and 3.09 ± 1.4 vessels/mm^2 for control and low-density and high-density flock scaffolds. Similarly, vessel counts at day 14 were 1.72 ± 0.43, 2.90 ± 0.69, and 4.89 ± 1.30 vessels/mm^2 for control and low-density and high-density flock scaffolds. Both between and within group significance was present at each time point ($P < 0.0001$, $n = 12$) (Fig. 7 F). From day 7–14, the high-density flock scaffold group experienced the most significant increase in vessel density ($P < 0.0001$, $n = 4$), followed by low-density flocked scaffolds ($P = 0.0069$, $n = 4$) and control groups ($P = 0.017$, $n = 4$). There are several explanations for the fiber-dependent angiogenesis observed, and it is possible a synergistic mechanism is at play. First, we note that the number of fibers within the wound decreases between days 7 and 14, which was the desired and expected outcome when using PGLA (90:10). PGLA has a notably fast degradation rate due to the smaller ratio of lactic acid (which increases hydrophobicity of the methyl group on the lactide monomer), and products of degradation are lactic and glycolic acid [56]. Previous studies indicated a positive relationship between lactic acid and angiogenesis/wound healing, which may explain the fiber density-dependent angiogenic effect observed [57]. In this study, sustained local lactate release from biodegradation of PLA and PLGA lead to reparative angiogenesis in superficial and ischemic wounds, and a similar effect may be at synergistic play in this scenario. In addition, mechanical perturbations and microstresses induced by the penetration and/or presence of flock fibers in the wound may trigger fiber density-dependent angiogenesis [58,59]. Granulation tissue formation, a hallmark in wound healing, is often subjectively measured [60, 61]. In this case, color deconvolution of TRI staining (Fig. S6 B) within the wound bed were used to quantify collagen deposition as a proxy measure of granulation tissue formation [62,63]. By day 7, control, low-density and high-density flock scaffolds reached integrated density values of $(3.12 \pm 0.93) \times 10^7$, $(4.72 \pm 0.90) \times 10^7$, and $(7.80 \pm 0.65) \times 10^7$ a.u., respectively ($P < 0.0014$, $n = 3$). By day 14, integrated density values achieved $(3.03 \pm 0.76) \times 10^7$, $(5.97 \pm 1.17) \times 10^7$, and $(9.93 \pm 2.14) \times 10^7$ a.u., respectively ($P < 0.0001$, $n = 3$) (Fig. 7 G). Another noteworthy observation is the decrease in fiber remnants between days 7 and 14 in all groups, indicating the PGLA (90:10) fibers may have suitable degradation profiles in vivo for wound healing. Daily gross anatomical examination revealed no superfluous production of wound exudate, changes in animal behavior, or noticeably different degrees of inflammation. Further, gross anatomical examination found that many fibers retained alignment in situ with tissue having formed around them. No significant differences in masses were noted between or within groups ($P = 0.7627$, $n = 4$) (Fig. S7).

3.6. Flock fiber-reinforced artificial vertebral discs are mechanically robust

To demonstrate how flocking may be used in a stress-shielding manner, a proof-of-concept AVD substitute utilizing flocked layers to emulate the angle-ply structure of the native disc was created using PLA flock reinforcement. AVDs were engineered based on anatomically-accurate vertebrae (Fig. 8A) with the goal of reinforcing elastomeric disc replacements (Fig. 8 B & C), which are one modality for disc replacement [64]. Pure PDMS (Fig. 8 D), isotropic (Fig. 8 E), and flocked (Fig. 8 F) discs were evaluated for several hallmark metrics as AVDs. Preliminary tests showed that all discs exhibited elastomeric behavior, returning to their original shape after compression, unless fracture occurred. Stress relaxation and dynamic tests were performed on the discs to characterize the difference in performance between pure elastomeric discs, isotropic reinforced discs, and flocked discs. Comprehensive stress-strain curves during loading and cyclic compression are presented in Fig. 8 G. The relaxation period was deemed sufficient because the equilibrium modulus had a variation of 0.1% or less in the last 10 s before the start of the cycles (Table 3). For each sample, the equilibrium modulus was calculated by dividing the stress at equilibrium by the strain at equilibrium [65]. The equilibrium modulus of the flocked (8017.8 kPa) disc at the end of the relaxation was almost double the modulus of the isotropic (4459.7 kPa) and the control (4649.6 kPa) disc. During loading, flocked discs required approximately 75% more load (2051 kPa) than the control (1290 kPa) and the isotropic (1226 kPa) discs to reach 20% strain (Fig. 8H). The stress amplitude during the cyclic loading was the highest for the flocked disc. Upon ramping, the flocked and isotropic discs exhibited a higher stiffness as compared to the control disc, as evident by their steeper loading curves. Though the control and the isotropic discs exhibited the same deformation and stress response at 20% strain and during cyclic loading, the flocked discs showed a higher stiffness only after 10% of the strain during the loading phase. This observation is supported by the strain energy in Table 3. The strain energy of the flocked discs (179.2 J) was more than twice the strain energy of the isotropic (80.5 J) and control (124.7 J) discs. The layer reinforcement in the flocked discs increased the resistance to deformation and isotropic strain after 10% strain. During the cyclic loading, all the samples exhibited the same phase lag response (Fig. 8 I). While the isotropic and the control discs exhibited the same stress response, the flocked discs considerably varied in stress amplitude within the 1% strain of cyclic loading. This observation is explained by the dissipated energy of the discs in the last 10 cycles. The dissipated energy is the area in the middle of the hysteresis loop. All samples had increasing stress dissipation during the first 10 cycles (Fig. 8 J), but it was observed that the flocked disc dissipated nearly twice the energy of the isotropic and control discs in the first and last 10 compressive cycles (Fig. 8 K & L) ($P < 0.0001$, $n = 10$). The consistency in dissipated energy in the last 10 cycles is an indicator that the hysteresis loops were aligned and there was minimal deviation in loading and unloading (Fig. 8 G). The anisotropy imparted by the flocked layers contribute to the increased stiffness and compressive strength, though the mechanical characteristics of the PDMS (i.e., hysteresis looping and elastomeric behavior) are retained. The ability of flock fibers to induce anisotropy in a biomedical elastomer has not yet been reported, though several studies have sought to use a similar framework to create ultra-strong composite materials and reinforce hydrogels [66,67]. In addition to the anisotropy of the flocked fibers, the use of layered flocked structures contributes to the bulk material toughness. In this case, the choice of an elastomer as the matrix may increase the durability of the AVD, which is a critically important consideration in designing AVDs [28]. Flock fiber reinforcement does not change the shape or surface finish of the elastomeric AVD and as a platform, could be built upon to create biologically-relevant flock-reinforced elastomer biomaterials for AVDs or other load-bearing applications.
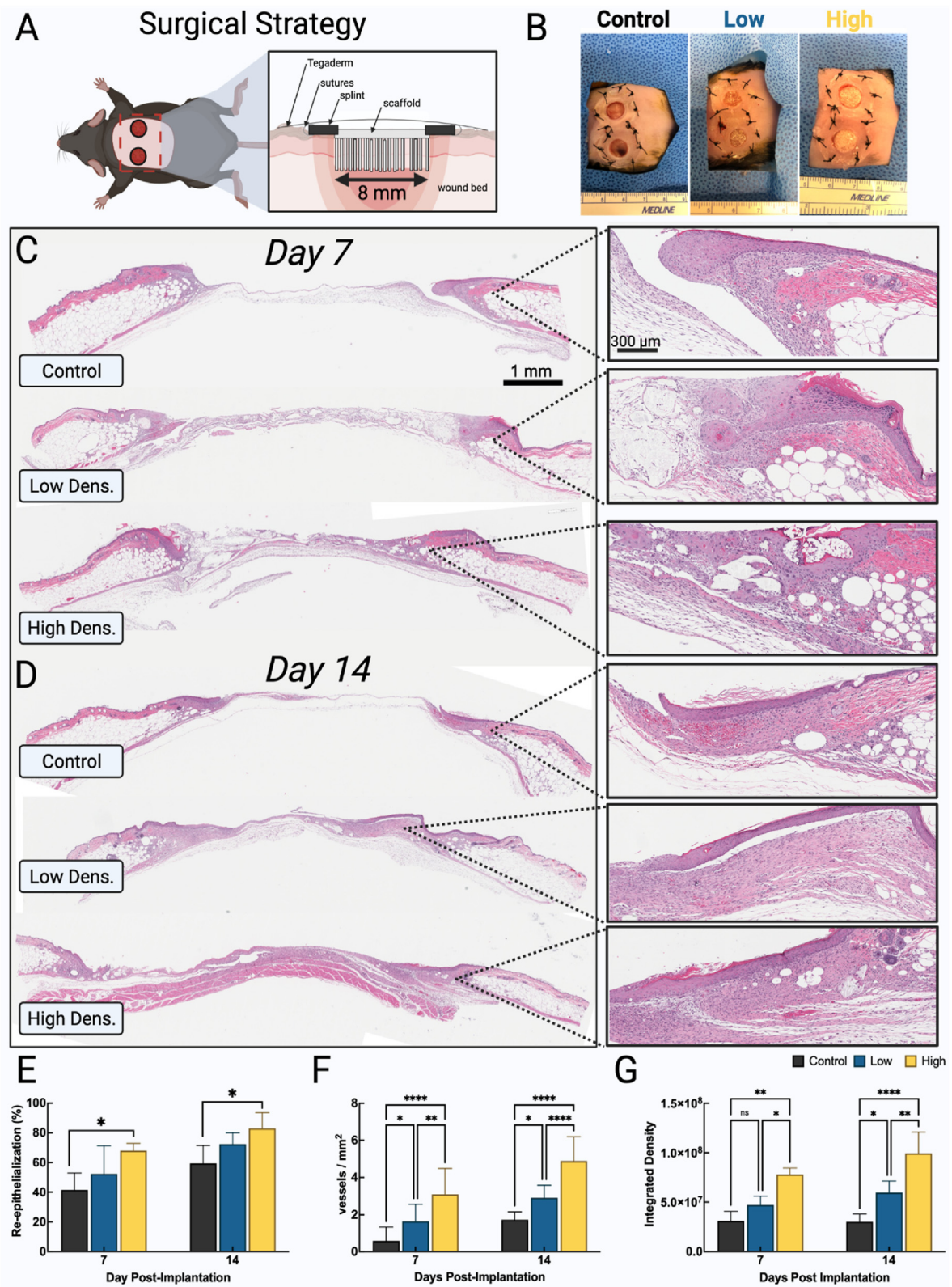
Fig. 7. Low- and high-density flocked scaffolds for wound healing. (A) Surgical strategy schematic. Flock fibers are positioned facing the wound bed and the chitosan/gelatin substrate is flush with the wound edge. Splints are glued and sutured into place to prevent wound contraction. (C, D) H&E staining of wounds after 7 and 14 days of no treatment, low-density flock scaffold treatment, and high-density flock scaffold treatment. (E) Re-epithelialization measured as the fraction of epithelium over the defect site. (F) New vessels formed within the wounds. (G) Collagen deposition within the wound measured via integrated density in color-split trichrome stained images. Control: without treatment; Low: low-density flocked scaffolds; High: high-density flocked scaffolds.
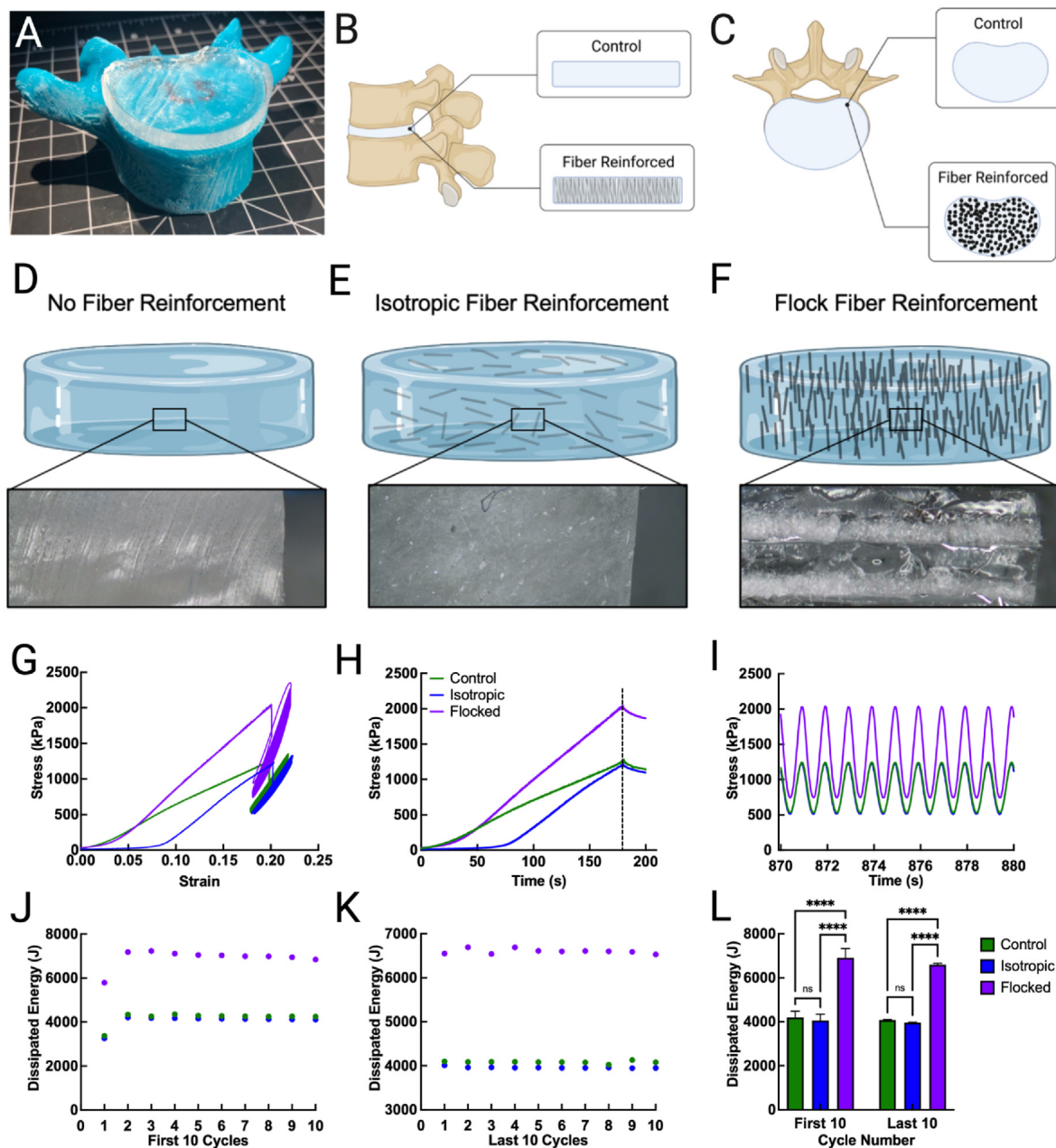
Fig. 8. Mechanical analysis of artificial vertebral disc (AVD) undergoing cyclic compressive loads. (A) Photograph of AVD situated on L5 model during sizing. (B, C) Representative (B) side and (C) top view of AVD in situ. (D–F) Schematic and cross-sectional microscopic image of (D) pure PDMS AVD, (E) isotropic fiber-reinforced AVD, and (F) flock fiber reinforced AVD. (G) Full stress-strain curve of each AVD model. (H) Stress curves during the first 3 min of compression (ramping). (I) Last 10 cyclic compressive loads to display waveform stress recovery. (J–L) Dissipation energy during (J) the first 10 and (K) last 10 compressive cycles and (L) their change between cycle sets.

Table 3
Mechanical characteristics of elastomeric disc replacements.

Model	Equilibrium Modulus (kPa)	△Equilibrium (% last 10 s)	Strain Energy (J)
Control Disc	4649.6	0.07	124.7
Isotropic Disc	4459.7	0.09	80.5
Flocked Disc	8017.8	0.1	179.2

4. Conclusion

The present study demonstrates several important proof-of-concept studies related to electrostatic flocking. First, a salt (NaCl)-based system for increasing surface charge accumulation on inherently electrostatically insulative polymer fibers is introduced. Conventional electrostatic flocking relies upon the ability of flocking fibers to accumulate sufficient charge for flocking. To accomplish this, previous studies have utilized inherently semi-conductive polymers or utilized a filling method. However, here, we demonstrate how simple salt ionization may be an effective alternative approach for charge accumulation. Because the salt treatment is confined to surface adhesion, simply washing the flocked objects with water allows for rapid and effective removal of salt residues. This methodology enables flocking of intrinsically-insulative polymers without utilization of cytotoxic or proprietary organic salt and aliphatic acid finishes. Future studies may investigate optimal salt loading concentrations to determine optimal treatments at different humidities. Second, for the first time, we report the electrostatic flocking of NFYs fabricated by rolling electrospun nanofiber strips. NFYs are mechanically robust, capable of flocking in quantities similar to MFs, and capable of releasing absorbed molecules. This opens the possibility of constructing flocked scaffolds with enhanced functionality via incorporation of drugs and other biologics. To highlight possible biomedical applications of electrostatic flocking, we cultured HaCaT cells on scaffolds and demonstrated the ability to modulate cell migration along the length of the fibers. To apply this towards a clinically relevant in vivo model, we replaced the PCL fibers with fast degrading PGLA (90:10) fibers and investigated it as a wound treatment in a diabetic mouse model. The results from the wound healing study affirmed the degradation of fibers and reaffirmed a fiber density-dependent effect with modest improvement in wound healing. Fibers induced granulation tissue formation and increased re-epithelization. Finally, to demonstrate how flocking can be used as a functional technique for inducing structural anisotropy, we synthesized a proof-of-concept, anatomically-accurate L4-L5 AVD. AVDs with flocked layers required 75% more load to achieve 20% strain than control and isotropic AVDs. Similarly, flocked AVDs dissipated more energy, had a higher equilibrium modulus, and retained elastomeric shape recovery after 100 supraphysiological compressive loads. Taken together, this study highlights several clinically relevant applications of a simple yet impactful flocking methodology. Future studies investigating salt-based flocking systems for environmental [68], solar [69], tissue engineering, and flock-reinforced hydrogels and elastomers are feasible and warranted.

Credit author statement

A.M., P.A.H. and D.B. synthesized, characterized, and fabricated all of the materials in this study. A.M., K.L., M.A., P.A.H., D.B., and J.L. conducted all of the mechanical experiments in this study. A.M. and A.K. conducted all of the in vitro studies. A.M., J.V.J., and S.W. conducted the animal surgeries. A.M. prepared the manuscript. J.X. reviewed and edited the manuscript.

Declaration of competing interest

The authors declare that they have no known competing financial interest or personal relationships that could have appeared to influence the work reported in this paper.

Acknowledgements

Appendix A. Supplementary data

Supplementary data to this article can be found online at https://doi.org/10.1016/j.mtbio.2021.100166.

References

[1] Y. Fang, Y. Xu, Z. Wang, W. Zhou, L. Yan, X. Fan, H. Liu, 3D porous chitin sponge with high absorbency, rapid shape recovery, and excellent antibacterial activities for noncompressible wound, Chem. Eng. J. 388 (2020) 124169, https://doi.org/10.1016/j.cej.2020.124169.

[2] S. Chen, H. Wang, A. McCarthy, Z. Yan, H.J. Kim, M.A. Carlson, Y. Xia, J. Xie, Three-dimensional objects consisting of hierarchically assembled nanofibers with controlled alignments for regenerative medicine, Nano Lett. 19 (2019) 2059–2065, https://doi.org/10.1021/acs.nanolett.9b00217.

[3] J.V. John, A. McCarthy, H. Wang, Z. Luo, H. Li, Z. Wang, F. Cheng, Y.S. Zhang, J. Xie, Freeze-casting with 3D-printed templates creates anisotropic microchannels and patterned macrochannels within biomimetic nanofiber aerogels for rapid cellular infiltration, Adv. Healthc. Mater. 12 (2021) 2100238, https://doi.org/10.1002/adhm.202100238.

[4] C. Wang, X. Chen, B. Wang, M. Huang, B. Wang, Y. Jiang, R.S. Ruoff, Freeze-casting produces a graphene oxide aerogel with a radial and centrosymmetric structure, ACS Nano 12 (2018) 5816–5825, https://doi.org/10.1021/acsnano.8b01747.

[5] P. Balasubramanian, A.R. Boccaccini, Bilayered bioactive glass scaffolds incorporating fibrous morphology by flock technology, Mater. Lett. 158 (2015) 313–316, https://doi.org/10.1016/j.matlet.2015.06.036.

[6] E. Gossla, R. Tonndorf, A. Bernhardt, M. Kirsten, R.-D. Hund, D. Aibibu, C. Cherif, M. Gelinsky, Electrostatic flocking of chitosan fibres leads to highly porous, elastic and fully biodegradable anisotropic scaffolds, Acta Biomater. 44 (2016) 267–276, https://doi.org/10.1016/j.actbio.2016.08.022.

[7] A. McCarthy, L. Saldana, D. McGoldrick, J.V. John, M. Kuss, S. Chen, B. Duan, M.A. Carlson, J. Xie, Large-scale synthesis of compressible and re-expandable three-dimensional nanofiber matrices, Nano Select 2 (2021) 1566–1579, https://doi.org/10.1002/nano.202000284.

[8] Y.K. Kim, Flocked fabrics and structures, in: Specialist Yarn and Fabric Structures, Elsevier, 2011, pp. 287–317, https://doi.org/10.1533/9780857093936.287.

[9] K. Uetani, S. Ata, S. Tomonoh, T. Yamada, M. Yumura, K. Hata, Elastomeric thermal interface materials with high through-plane thermal conductivity from carbon fiber fillers vertically aligned by electrostatic flocking, Adv. Mater. 26 (2014) 5857–5862, https://doi.org/10.1002/adma.201401736.

[10] R. Tonndorf, E. Gossla, R.T. Kocaman, M. Kirsten, R.-D. Hund, G. Hoffmann, D. Aibibu, M. Gelinsky, C. Cherif, Factors affecting the mechanical and geometrical properties of electrostatically flocked pure chitosan fiber scaffolds, Textil. Res. J. 88 (2018) 1965–1978, https://doi.org/10.1177/0040517517715083.

[11] A. Walther, B. Hoyer, A. Springer, B. Mrozik, T. Hanke, C. Cherif, W. Pompe, M. Gelinsky, Novel textile scaffolds generated by flock technology for tissue engineering of bone and cartilage, Materials 5 (2012) 540–557, https://doi.org/10.3390/ma5030540.

[12] A. McCarthy, J.V. John, L. Saldana, H. Wang, M. Lagerstrom, S. Chen, Y. Su, M. Kuss, B. Duan, M.A. Carlson, J. Xie, Electrostatic flocking of insulative and biodegradable polymer microfibers for biomedical applications, Adv. Healthc. Mater. (2021) 2100766, https://doi.org/10.1002/adhm.202100766.

[13] R.F. Gouveia, F. Galembeck, Electrostatic charging of hydrophilic particles due to water adsorption, J. Am. Chem. Soc. 131 (2009) 11381–11386, https://doi.org/10.1021/ja900704f.

[14] S. Kim, S. Choi, E. Oh, J. Byun, H. Kim, B. Lee, S. Lee, Y. Hong, Revisit to three-dimensional percolation theory: accurate analysis for highly stretchable conductive composite materials, Sci. Rep. 6 (2016) 34632, https://doi.org/10.1038/srep34632.

[15] W. Ingamells, N. Ramadan, The influence of finishing agents on the performance of fibres during electrostatic flocking, J. Soc. Dye. Colour. 108 (2008) 270–278, https://doi.org/10.1111/j.1478-4408.1992.tb01460.x.

[16] H. Golnabi, M.R. Matloob, M. Bahar, M. Sharifian, Investigation of electrical conductivity of different water liquids and electrolyte solutions, Iran, Phys. J. 3 (2009) 6.

[17] K. Kiran, M. Ravi, Y. Pavani, S. Bhavani, A.K. Sharma, V.V.R. Narasimha Rao, Electrical conduction mechanism in NaCl complexed PEO/PVP polymer blend electrolytes, J. Non-Cryst. Solids 358 (2012) 3205–3211, https://doi.org/10.1016/j.jnoncrysol.2012.08.022.

[18] G. Lu, Z. Ding, Y. Wei, X. Lu, Q. Lu, D.L. Kaplan, Anisotropic biomimetic silk scaffolds for improved cell migration and healing of skin wounds, ACS Appl. Mater. Interfaces 10 (2018) 44314–44323, https://doi.org/10.1021/acsami.8b18626.

[19] S. Chen, H. Wang, Y. Su, J.V. John, A. McCarthy, S.L. Wong, J. Xie, Mesenchymal stem cell-laden, personalized 3D scaffolds with controlled structure and fiber

alignment promote diabetic wound healing, Acta Biomater. 108 (2020) 153–167, https://doi.org/10.1016/j.actbio.2020.03.035.

[20] A. Landsman, A. Masturzo, A. Barbul, PIT9 Examining the real-world healthcare costs of treating chronic wounds, Value Health 22 (2019) S213, https://doi.org/10.1016/j.jval.2019.04.981.

[21] G. Han, R. Ceilley, Chronic wound healing: a review of current management and treatments, Adv. Ther. 34 (2017) 599–610, https://doi.org/10.1007/s12325-017-0478-y.

[22] Z. Yu, S. Wei, J. Guo, Fabrication of aligned carbon-fiber/polymer TIMs using electrostatic flocking method, J. Mater. Sci. Mater. Electron. 30 (2019) 10233–10243, https://doi.org/10.1007/s10854-019-01360-7.

[23] R.H. Volpe, D. Mistry, V.V. Patel, R.R. Patel, C.M. Yakacki, Dynamically crystalizing liquid-crystal elastomers for an expandable endplate-conforming interbody fusion cage, Adv. Healthc. Mater. 9 (2020), e1901136, https://doi.org/10.1002/adhm.201901136.

[24] M. Khandaker, S. Riahinazad, Evaluation of electrospun nanofiber-anchored silicone for the degenerative intervertebral disc, J. Healthc. Eng. (2017) 5283846, https://doi.org/10.1155/2017/5283846, 2017.

[25] J. Dowdell, M. Erwin, T. Choma, A. Vaccaro, J. Iatridis, S.K. Cho, Intervertebral disk degeneration and repair, Neurosurgery 80 (2017) S46–S54, https://doi.org/10.1093/neuros/nyw078.

[26] M.D. Humzah, R.W. Soames, Human intervertebral disc: structure and function, Anat 220 (1988) 337–356, https://doi.org/10.1002/ar.1092200402.

[27] H.S. Kim, P.H. Wu, I.-T. Jang, Lumbar degenerative disease Part 1: anatomy and pathophysiology of intervertebral discogenic pain and radiofrequency ablation of basivertebral and sinuvertebral nerve treatment for chronic discogenic back pain: a prospective case series and review of literature, Int. J. Mol. Sci. 21 (2020) 1483, https://doi.org/10.3390/ijms21041483.

[28] J.T. Martin, A.H. Milby, J.A. Chiaro, D.H. Kim, N.M. Hebela, L.J. Smith, D.M. Elliott, R.L. Mauck, Translation of an engineered nanofibrous disc-like angle-ply structure for intervertebral disc replacement in a small animal model, Acta Biomater. 10 (2014) 2473–2481, https://doi.org/10.1016/j.actbio.2014.02.024.

[29] L.J. Smith, N.L. Fazzalari, The elastic fibre network of the human lumbar anulus fibrosus: architecture, mechanical function and potential role in the progression of intervertebral disc degeneration, Eur. Spine J. 18 (2009) 439–448, https://doi.org/10.1007/s00586-009-0918-8.

[30] C. Formica, A. Zanirato, S. Divano, M. Basso, L. Cavagnaro, M. Alessio Mazzola, V.G. Vellone, M. Mastrogiacomo, P. Berjano, L. Felli, M. Formica, Total disc replacement for lumbar degenerative disc disease: single centre 20 years experience, Eur. Spine J. 29 (2020) 1518–1526, https://doi.org/10.1007/s00586-019-06100-3.

[31] S.N. Salzmann, N. Plais, J. Shue, F.P. Girardi, Lumbar disc replacement surgery—successes and obstacles to widespread adoption, Curr. Rev. Musculoskelet. Med. 10 (2017) 153–159, https://doi.org/10.1007/s12178-017-9397-4.

[32] Y.A. Othman, R. Verma, S.A. Qureshi, Artificial disc replacement in spine surgery, Ann. Transl. Med. 7 (2019), https://doi.org/10.21037/atm.2019.08.26.

[33] S. Chen, L. Ge, A. Mueller, M.A. Carlson, M.J. Teusink, F.D. Shuler, J. Xie, Twisting electrospun nanofiber fine strips into functional sutures for sustained co-delivery of gentamicin and silver, Nanomedicine 13 (2017) 1435–1445, https://doi.org/10.1016/j.nano.2017.01.016.

[34] R. Rezakhaniha, A. Agianniotis, J.T.C. Schrauwen, A. Griffa, D. Sage, C.V.C. Bouten, F.N. van de Vosse, M. Unser, N. Stergiopulos, Experimental investigation of collagen waviness and orientation in the arterial adventitia using confocal laser scanning microscopy, Biomech. Model. Mechanobiol. 11 (2012) 461–473, https://doi.org/10.1007/s10237-011-0325-z.

[35] S.C.L. Fischer, O. Levy, E. Kroner, R. Hensel, J.M. Karp, E. Arzt, Bioinspired polydimethylsiloxane-based composites with high shear resistance against wet tissue, J. Mech. Behav. Biomed. Mater. 61 (2016) 87–95, https://doi.org/10.1016/j.jmbbm.2016.01.014.

[36] A.G. Alvarez, K.D. Dearn, D.E.T. Shepherd, Design and material evaluation for a novel lumbar disc replacement implanted via unilateral transforaminal approach, J. Mech. Behav. Biomed. Mater. 91 (2019) 383–390, https://doi.org/10.1016/j.jmbbm.2018.12.011.

[37] F.J. Onishi, M.A. de Paiva Neto, S. Cavalheiro, R.S. Centeno, Morphometric analysis of 900 lumbar intervertebral discs: anterior and posterior height analysis and their ratio, Interdiscip. Neurosurg. 18 (2019) 100523, https://doi.org/10.1016/j.inat.2019.100523.

[38] S.H. Zhou, I.D. McCarthy, A.H. McGregor, R.R. Coombs, S.P. Hughes, Geometrical dimensions of the lower lumbar vertebrae–analysis of data from digitised CT images, Eur. Spine J. 9 (2000) 242–248, https://doi.org/10.1007/s005860000140.

[39] E.M. Steele, D.S. Steele, Automated detection and analysis of Ca^{2+} sparks in x-y image stacks using a thresholding algorithm implemented within the open-source image analysis platform ImageJ, Biophys. J. 106 (2014) 566–576, https://doi.org/10.1016/j.bpj.2013.12.040.

[40] D.S. Masson-Meyers, T.A.M. Andrade, G.F. Caetano, F.R. Guimaraes, M.N. Leite, S.N. Leite, M.A.C. Frade, Experimental models and methods for cutaneous wound healing assessment, Int. J. Exp. 101 (2020) 21–37, https://doi.org/10.1111/iep.12346.

[41] Y. Chen, Q. Yu, C.-B. Xu, A convenient method for quantifying collagen fibers in atherosclerotic lesions by ImageJ software, Int. J. Clin. Exp. Med. 10 (2017) 14904–14910.

[42] C.M. Hwang, Y. Park, J.Y. Park, K. Lee, K. Sun, A. Khademhosseini, S.H. Lee, Controlled cellular orientation on PLGA microfibers with defined diameters, Biomed. Microdevices 11 (2009) 739–746, https://doi.org/10.1007/s10544-009-9287-7.

[43] S. Chen, L. Ge, A.F. Gombart, F.D. Shuler, M.A. Carlson, D.A. Reilly, J. Xie, Nanofiber-based sutures induce endogenous antimicrobial peptide, Nanomedicine 12 (2017) 2597–2609, https://doi.org/10.2217/nnm-2017-0161.

[44] H. Maleki, A.A. Gharehaghaji, T. Toliyat, P.J. Dijkstra, Drug release behavior of electrospun twisted yarns as implantable medical devices, Biofabrication 8 (2016) 035019, https://doi.org/10.1088/1758-5090/8/3/035019.

[45] A. Sohrabi, P.M. Shaibani, H. Etayash, K. Kaur, T. Thundat, Sustained drug release and antibacterial activity of ampicillin incorporated poly(methyl methacrylate)–nylon6 core/shell nanofibers, Polymer 54 (2013) 2699–2705, https://doi.org/10.1016/j.polymer.2013.03.046.

[46] J. Paulose, D.R. Nelson, J. Aizenberg, Two-parameter sequential adsorption model applied to microfiber clustering, Soft Matter 6 (2010) 2421–2434, https://doi.org/10.1039/C000443J.

[47] J. Liu, H. Zhai, Y. Sun, S. Wu, S. Chen, Developing high strength poly($_L$-lactic acid) nanofiber yarns for biomedical textile materials: a comparative study of novel nanofiber yarns and traditional microfiber yarns, Mater. Lett. 300 (2021) 130229, https://doi.org/10.1016/j.matlet.2021.130229.

[48] O. Verschatse, L. Daelemans, W. Van Paepegem, K. De Clerck, In-situ observations of microscale ductility in a quasi-brittle bulk scale epoxy, Polymers 12 (2020) 2581, https://doi.org/10.3390/polym12112581.

[49] D.A. Brennan, A.A. Conte, G. Kanski, S. Turkula, X. Hu, M.T. Kleiner, V. Beachley, Mechanical considerations for electrospun nanofibers in tendon and ligament repair, Adv. Healthc. Mater. 7 (2018) 1701277, https://doi.org/10.1002/adhm.201701277.

[50] S. Russo, T. Ranzani, H. Liu, S. Nefti-Meziani, K. Althoefer, A. Menciassi, Soft and stretchable sensor using biocompatible electrodes and liquid for medical applications, Soft Robot. 2 (2015) 146–154, https://doi.org/10.1089/soro.2015.0011.

[51] F. Chayad, A. Jabur, N. Jalal, Effect of NaCl solution addition on improving some of the physical properties of nylon 6 solutions used for electro spinning purpose, J. Eng. Technol. 34 (2016) 1265–1274.

[52] S. Zhao, P. Tseng, J. Grasman, Y. Wang, W. Li, B. Napier, B. Yavuz, Y. Chen, L. Howell, J. Rincon, F.G. Omenetto, D.L. Kaplan, Programmable hydrogel ionic circuits for biologically matched electronic interfaces, Adv. Mater. 30 (2018) 1800598, https://doi.org/10.1002/adma.201800598.

[53] Y. Xia, J. Ouyang, Salt-induced charge screening and significant conductivity enhancement of conducting poly(3,4-ethylenedioxythiophene): poly(styrenesulfonate), Macromolecules 42 (2009) 4141–4147, https://doi.org/10.1021/ma900327d.

[54] J. Ouyang, Q. Xu, C.-W. Chu, Y. Yang, G. Li, J. Shinar, On the mechanism of conductivity enhancement in poly(3,4-ethylenedioxythiophene):poly(styrene sulfonate) film through solvent treatment, Polymer 45 (2004) 8443–8450, https://doi.org/10.1016/j.polymer.2004.10.001.

[55] B. Zhen, M. Buszko, G. Cappellano, G. Wick, Elevated sodium leads to the increased expression of HSP60 and induces apoptosis in HUVECs, PLoS One 12 (2017), e0179383, https://doi.org/10.1371/journal.pone.0179383.

[56] H.K. Makadia, S.J. Siegel, Poly lactic-co-glycolic acid (PLGA) as biodegradable controlled drug delivery carrier, Polymers 3 (2011) 1377–1397, https://doi.org/10.3390/polym3031377.

[57] P.E. Porporato, V.L. Payen, C.J. De Saedeleer, V. Preat, J.-P. Thissen, O. Feron, P. Sonveaux, Lactate stimulates angiogenesis and accelerates the healing of superficial and ischemic wounds in mice, Angiogenesis 4 (2012) 581–592, https://doi.org/10.1007/s10456-012-9282-0.

[58] H. Liebl, L.C. Kloth, Skin cell proliferation stimulated by microneedles, J. Am. Coll. Clin. Wound Spec. 4 (2012) 2–6, https://doi.org/10.1016/j.jccw.2012.11.001.

[59] M. Kathryn Sewell-Loftin, J.B. Katz, S.C. George, G.D. Longmore, Micro-strains in the extracellular matrix induce angiogenesis, Lab Chip 20 (2020) 2776–2787, https://doi.org/10.1039/D0LC00145G.

[60] A. Giacaman Fonseca, Development of Bioactive Electrospun Scaffolds to Support Granulation Tissue Formation in Non-healing Wounds, Ph.D. Thesis, University of Nottingham, 2018, http://eprints.nottingham.ac.uk/51389.

[61] Y. Wang, R. Xu, G. Luo, Q. Lei, Q. Shu, Z. Yao, H. Li, J. Zhou, J. Tan, S. Yang, R. Zhan, W. He, J. Wu, Biomimetic fibroblast-loaded artificial dermis with "sandwich" structure and designed gradient pore sizes promotes wound healing by favoring granulation tissue formation and wound re-epithelialization, Acta Biomater. 30 (2016) 246–257, https://doi.org/10.1016/j.actbio.2015.11.035.

[62] L.N. Jørgensen, Collagen deposition in the subcutaneous tissue during wound healing in humans: a model evaluation, APMIS Suppl. 115 (2003) 1–56.

[63] N.A.J. Cremers, M. Suttorp, M.M. Gerritsen, R.J. Wong, C. van Run-van Breda, G.M. van Dam, K.M. Brouwer, A.M. Kuijpers-Jagtman, C.E.L. Carels, D.M.S. Lundvig, F.A.D.T.G. Wagener, Mechanical stress changes the complex interplay between HO-1, inflammation and fibrosis, during excisional wound repair, Front. Med. 2 (2015), https://doi.org/10.3389/fmed.2015.00086.

[64] L. Pimenta, R. Springmuller, C.K. Lee, L. Oliveira, S.E. Roth, W.F. Ogilvie, Clinical performance of an elastomeric lumbar disc replacement: minimum 12 months follow-up, SAS J 4 (2010) 16–25, https://doi.org/10.1016/j.esas.2009.12.002.

[65] J.M. Patel, B.C. Wise, E.D. Bonnevie, R.L. Mauck, A systematic review and guide to mechanical testing for articular cartilage tissue engineering, Tissue Eng. Part C Methods 25 (2019) 593–608, https://doi.org/10.1089/ten.tec.2019.0116.

[66] E. Gossla, A. Bernhardt, R. Tonndorf, D. Aibibu, C. Cherif, M. Gelinsky, Anisotropic chitosan scaffolds generated by electrostatic flocking combined with alginate hydrogel support chondrogenic differentiation, Indian J. Manag. Sci. 22 (2021) 9341, https://doi.org/10.3390/ijms22179341.

[67] Y. Kim, J.M. Rice, V. Chalivendra, A.F. Lewis, Flock fibre-reinforced laminar composites for improved mode I fracture toughness, JEC Compos. 54 (2017) 48–53.

[68] X. Xu, K. Wang, H. Guo, G. Sun, R. Chen, J. Yu, J. Liu, C. Lin, J. Wang, Zwitterionic modified electrostatic flocking surfaces for diatoms and mussels resistance, J. Colloid Interface Sci. 588 (2021) 9–18, https://doi.org/10.1016/j.jcis.2020.12.036.

[69] C. Tu, W. Cai, X. Chen, X. Ouyang, H. Zhang, Z. Zhang, A 3D-structured sustainable solar-driven steam generator using super-black nylon flocking materials, Small 15 (2019) 1902070, https://doi.org/10.1002/smll.201902070.